

Constraints on fault slip rates of the southern California plate boundary from GPS velocity and stress inversions

Thorsten W. Becker,^{1,*} Jeanne L. Hardebeck² and Greg Anderson³

¹*Cecil H. and Ida M. Green Institute of Geophysics and Planetary Physics, Scripps Institution of Oceanography, University of California, San Diego 9500 Gilman Drive, La Jolla CA 92093, USA*

²*United States Geological Survey, 345 Middlefield Road, MS 977, Menlo Park, CA 94025, USA*

³*UNAVCO, Inc., 6350 Nautilus Drive, Boulder, CO 80301, USA*

Accepted 2004 November 18. Received 2004 November 10; in original form 2004 May 25

SUMMARY

We use Global Positioning System (GPS) velocities and stress orientations inferred from seismicity to invert for the distribution of slip on faults in the southern California plate-boundary region. Of particular interest is how long-term slip rates are partitioned between the Indio segment of the San Andreas fault (SAF), the San Jacinto fault (SJF) and the San Bernardino segment of the SAF. We use two new sets of constraints to address this problem. The first is geodetic velocities from the Southern California Earthquake Center's (SCEC) Crustal Motion Map (version 3 by Shen *et al.*), which includes significantly more data than previous models. The second is a regional model of stress-field orientations at seismogenic depths, as determined from earthquake focal mechanisms. While GPS data have been used in similar studies before, this is the first application of stress-field observations to this problem. We construct a simplified model of the southern California fault system, and estimate the interseismic surface velocities using a backslip approach with purely elastic strain accumulation, following Meade *et al.* In addition, we model the stress orientations at seismogenic depths, assuming that crustal stress results from the loading of active faults. The geodetically derived stressing rates are found to be aligned with the stress orientations from seismicity. We therefore proceed to invert simultaneously GPS and stress observations for slip rates of the faults in our network. We find that the regional patterns of crustal deformation as imaged by both data sets can be explained by our model, and that joint inversions lead to better constrained slip rates. In our preferred model, the SJF accommodates $\sim 15 \text{ mm yr}^{-1}$ and the Indio segment of the SAF $\sim 23 \text{ mm yr}^{-1}$ of right-lateral motion, accompanied by a low slip rate on the San Bernardino segment of the SAF. 'Anomalous' fault segments such as around the 1992 $M_w = 7.3$ Landers surface rupture can be detected. There, observed stresses deviate strongly from the long-term loading as predicted by our simple model. Evaluation of model misfits together with information from palaeoseismology may provide further insights into the time dependence of strain accumulation along the San Andreas system.

Key words: crustal deformation, crustal stress, fault slip rates, GPS, San Andreas, seismic hazard.

1 INTRODUCTION

The San Andreas fault (SAF) system is the most extensively studied and best instrumented strike-slip plate boundary on Earth. It is also a complex system with many fault segments of various orientations. Understanding how deformation and slip rates are partitioned between fault segments at the present-day and in the past is therefore

a major challenge. Better constraints on relative motions between the crustal blocks that are defined by the major faults will improve our knowledge of the mechanics of the SAF system, which has immediate implications for seismic hazard assessment.

Here, we focus on the southern California region of the SAF (Fig. 1), specifically on the distribution of long-term slip on the Indio and San Bernardino (SBM) segments of the SAF, the San Jacinto fault (SJF), and the eastern California shear zone (ECSZ). Slip rates in this region have been the subject of much debate (e.g. McGill *et al.* 2002), especially the partitioning of the $\sim 35 \text{ mm yr}^{-1}$ of slip in the southern region between the Indio segment of the SAF

*Now at: Department of Earth Sciences, University of Southern California, Los Angeles 90089-0740, USA. E-mail: twb@usc.edu

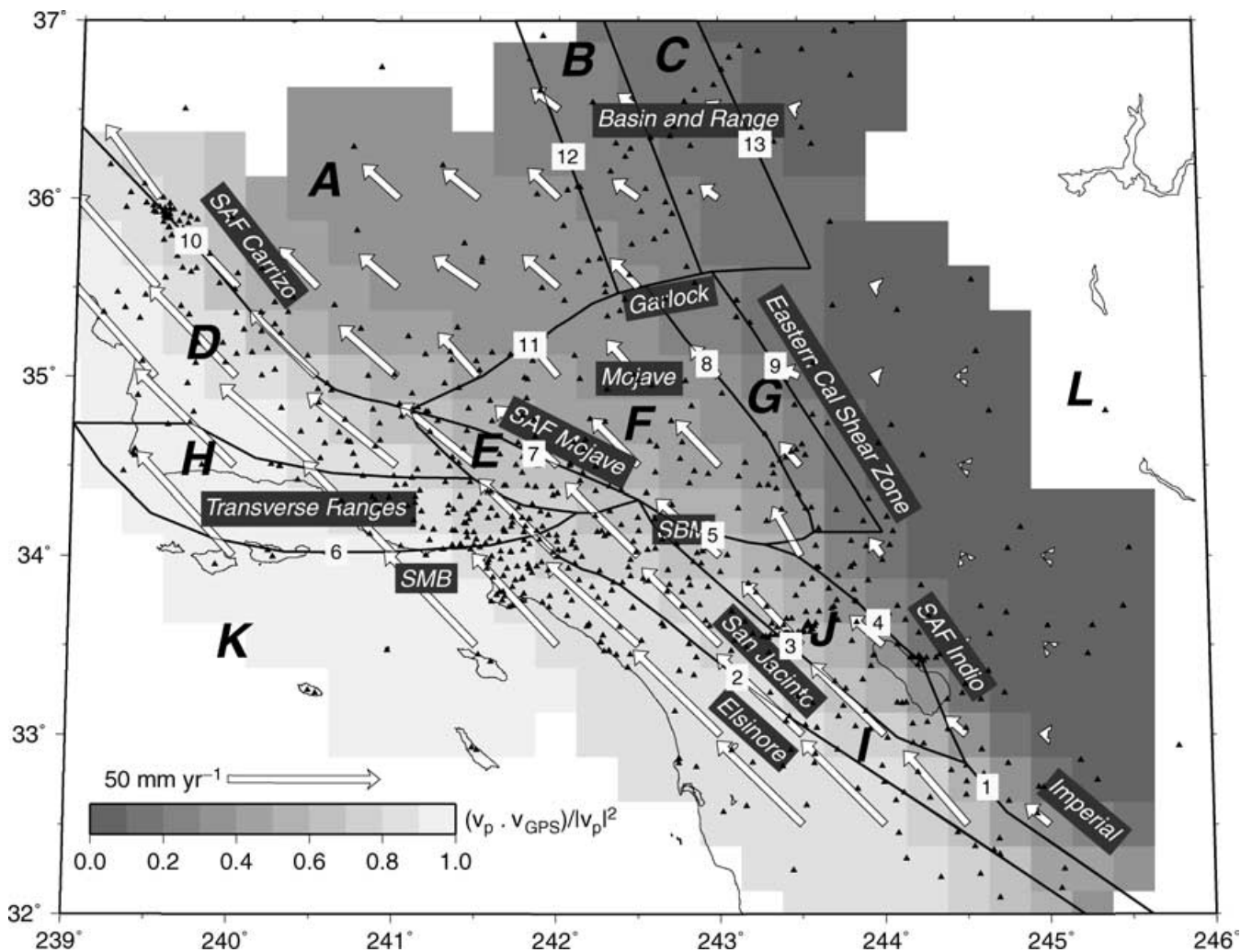


Figure 1. Crustal velocities in southern California for selected data from the SCEC Crustal Motion Map, version 3 (Shen *et al.* 2003); major fault strands and some geographic regions are also indicated. Abbreviations: SAF: San Andreas fault, SBM: San Bernardino Mountains, SMB: Santa Monica Bay. We show interpolated velocities, v_{GPS} , for visualization purposes [white vectors shown every 0.5° based on a $0.25^\circ \times 0.25^\circ$ grid generated by the GMT 'nearneighbor' algorithm (Wessel & Smith 1991) with a quadrant search radius of 0.65°], 533 selected sites as used for the inversion (triangles), our block model geometry (thick lines, see Section 2.3.4), and the normalized projection of v_{GPS} onto the relative rigid-plate velocities, v_p , between the North American and the Pacific plates from NUVEL1-A (DeMets *et al.* 1994), $(v_{GPS} \cdot v_p) / |v_p|^2$ (cf. Wdowinski *et al.* 2001). Small number labels with white background indicate segment codes as used in Table 1; larger letter labels denote block code.

and the SJF. One proposed model places $\sim 20\text{--}26 \text{ mm yr}^{-1}$ on the Indio segment of the SAF and $\sim 9\text{--}15 \text{ mm yr}^{-1}$ on the SJF, based on geological (Sharp 1981; Prentice *et al.* 1986; Rockwell *et al.* 1990) and geodetic (Bennett *et al.* 1996; Bourne *et al.* 1998) observations. In this model, the majority of the slip south of the SBM is on the Indio segment. This slip is transferred through the SBM segment of the SAF, with a predicted slip rate of $\sim 15 \text{ mm yr}^{-1}$ on that segment, and the remaining $\sim 8 \text{ mm yr}^{-1}$ being taken up in the ECSZ Peltzer *et al.* (2001).

An alternative model divides the slip more equally between the Indio SAF and the SJF. Brown (1990) gives a geological slip rate of $10\text{--}17 \text{ mm yr}^{-1}$ for the SJF, while Kendrick *et al.* (2002) argue for at least 20 mm yr^{-1} along the northern SJF. Recent work by Dorsey (2003) re-evaluates the slip-rate estimate of Keller *et al.* (1982) for the Indio segment of the SAF, and gives a new slip rate of $15 \pm 3 \text{ mm yr}^{-1}$ (1σ). Geodetic results support this model; the slip rate on the SJF is larger than on the SAF in Johnson's (1993) initial inversion and the more comprehensive approach of Meade *et al.*

(2002a). A reasonable model thus has slip rates of $\sim 15\text{--}20 \text{ mm yr}^{-1}$ on both the Indio SAF and the SJF. Again, $\sim 8 \text{ mm yr}^{-1}$ is taken up in the ECSZ, leaving $\sim 5\text{--}10 \text{ mm yr}^{-1}$ transferred through the SBM segment to the Mojave segment of the SAF. Discriminating between these scenarios is clearly important for estimating the seismic hazard arising from these faults.

We show that a joint inversion of geodetic velocities and stresses inverted from focal mechanisms can put further constraints on slip partitioning in this region. Our estimates of velocity gradients across the study region are based on a simplified crustal block model (Savage & Burford 1973), in which interseismic strain accumulation is taken up on faults that are locked. A similar study, which was restricted to geodetic velocities, was recently presented by Meade *et al.* (2002a). Our method is different in that we include stress data for the first time and use a different parametrization. We will compare results for geodetic inversions with more than one model geometry for southern California, and we will discuss the possible origin of disagreement between the models.

2 DATA AND METHOD

2.1 Crustal velocities

We use crustal velocities as provided by the SCEC Crustal Motion Map, version 3 (Shen *et al.* 2003). This data set consists of 828 independent geodetically determined velocities [survey and continuous GPS, VLBI, trilateration (EDM)], in a reference frame that was computed relative to 12 ‘stable North America’ GPS sites. Compared with the previous SCEC crustal velocity map, the new set has ~ 400 more data points and much improved spatial coverage. We edited the SCEC data set to exclude post-seismic transients, which are most significant around the 1992 $M_w = 7.3$ Landers event. Furthermore, we removed all VLBI and most EDM data because the latter show trends significantly different from surrounding GPS measurements in the Parkfield area. We will refer to the edited SCEC velocity model as ‘GPS velocities’ for brevity. We have also excluded some data from the dense GPS networks around Parkfield and Anza for a more uniform spatial coverage, and have removed those GPS stations that either we or Shen *et al.* (2003) identified as potential outliers, possibly related to site or post-seismic effects (Fig. 1 and Appendix). The main effect of excluding outliers is to reduce the formal misfit of the inversion (Section 3.1). We have verified that our results are stable with respect to data selection; inversions performed with the full data set lead to similar results with respect to fault slip rates.

Our block geometry is such that there are at least eight data points in each block, with fewest sites in block C. Seven out of the total of 540 GPS points of our edited SCEC data set are outside the study region, as shown in Fig. 1. We therefore have $n_{\text{GPS}} = 533$ velocity observations, with $v_{\text{GPS}} = n_{\text{GPS}} \times 2$ horizontal components (no vertical motions are included in the SCEC model). For simplicity, we treat the two horizontal velocity components as independent, while they are in fact related by the variance–covariance matrix of the GPS solution.

Fig. 1 shows the well-known transition of GPS velocities, v_{GPS} , from far-field Pacific plate motion to stable North America (e.g. Bennett *et al.* 1999). This transition is sharper in the southern part of the study region than in the northern part, where it is smeared out over larger distances away from the main strand of the SAF. The mean 1σ uncertainty of the magnitude of our GPS velocity vectors is $\approx 2 \text{ mm yr}^{-1}$ based on the SCEC standard errors, which is ≈ 6 per cent of the mean magnitude of the vector velocities. The mean 1σ uncertainty on the individual horizontal-component velocities is 1 mm yr^{-1} . Uncertainties are larger towards the east, and are particularly high around the San Bernardino mountains ($\sigma_v \sim 4 \text{ mm yr}^{-1}$).

We choose to present our results with respect to stable block L (see Fig. 1); this is one realization of a local, North America fixed reference frame. The rigid-body rotation we determined for L from the SCEC data away from known faults before the inversion based on GPS sites NEED, 0809, and 0801 is $\omega_r^L = (-0.007, 0.005, -0.02)^\circ \text{ Myr}^{-1}$ in a Cartesian system. This corresponds to a rotation pole and rate of $143.04^\circ \text{ E}/-66.58^\circ \text{ N } 0.02^\circ \text{ Myr}^{-1}$ in geographic coordinates, where x , y , and z are axes at $0^\circ \text{ E}/0^\circ \text{ N}$, $90^\circ \text{ E}/0^\circ \text{ N}$, and the geographic North pole, 90° N , respectively. During the inversion, we allow block L to readjust the reference frame by treating the long-term block motion, ω^L , as a free parameter (see Section 2.3.1 and Tables A1 and A2). This procedure leads to very similar relative block motions and model misfits when compared with an alternative approach in which we subtract ω_r^L from the SCEC velocities first and set ω^L constant and identical to zero.

2.2 Stress orientations from focal mechanisms

There are few direct observations of crustal stress (e.g. Zoback 1992; Reinecker *et al.* 2003), and such measurements are typically confined to shallow depths of $\lesssim 1 \text{ km}$. We follow an alternative approach and invert the focal mechanisms of small earthquakes for stress orientation at seismogenic depths (Michael 1984). We use a high-quality regional focal mechanism catalogue of ~ 5500 events computed using the technique of Hardebeck & Shearer (2002). Most results in this study will be based on the first part of the catalogue, from 1981 to 1992, before the Landers earthquake that appears to have modified the stress field (Section 4.4). Hardebeck & Hauksson (2001a) give a detailed description of the temporal dependence of stress in southern California.

We invert for stress orientation on an evenly spaced grid ($0.1^\circ \times 0.1^\circ$) and assign each earthquake to the nearest grid point. We use the inversion technique of Michael (1984), and estimate the uncertainties in the stress tensor components by bootstrap resampling (Michael 1987). This method has been shown to produce accurate stress orientations with reasonable uncertainty estimates (Hardebeck & Hauksson 2001b). We note that there are no assumptions about the frictional behaviour of faults in the inversion. However, results only constrain four out of six components of the stress tensor, τ : we have no constraints on the absolute magnitude or the isotropic component of stress. Consequently the maximum shear stress, $\tau_1 - \tau_3$, is set to unity and the trace of τ to zero. Here, τ_1 and τ_3 denote the largest and the smallest eigenvalue of τ , respectively, with tension taken positive.

Since we are aiming for a regional representation of crustal stress, we include a flatness constraint for the inversion, minimizing the difference between stress tensor components at adjacent gridpoints (Fig. 2). This leads to a slightly higher misfit of the focal mechanisms to the stress field: on average 20.5° in rake, compared with 19.5° for a model with no smoothing. A misfit of 20.5° is relatively low and indicates that the stress field at each gridpoint is homogeneous enough to be reliably found by inversion (Michael 1987). For the small 1° increase in misfit, we obtain a considerably smoother stress field compared with the results of Hardebeck & Hauksson (2001a), demonstrating that the spatial heterogeneity removed by the inversion damping was not strongly required by the data. Increasing the damping further would significantly increase the misfit, implying that the remaining spatial stress variations in our model are required by the focal mechanism data. The characteristic length scales of spatial stress variation that result from the smoothed model are $\sim 50 \text{ km}$; and the 1σ uncertainties of the orientation of the maximum horizontal stress axis, τ_1^h , are $\sim 15^\circ$.

Fig. 2 compares the results of a Kostrov (1974)-type summation of seismic moment tensors and of a stress inversion of our catalogue from 1981 up to the time of the Landers event in 1992. In Fig. 2(a), deviations from the right-lateral strike-slip regime are mostly found in the Transverse Ranges. Comparison of the stress inversion in Fig. 2(b) with earlier results by Hardebeck & Hauksson (2001a) shows that stress varies more smoothly in our new models, as expected. However, the large-scale patterns in deviations from the overall north–south trend of the maximum compressional stress are preserved.

There are several potential difficulties with the interpretation of interseismic moment release as a strain-rate field, or as being indicative of stress. When using a Kostrov (1974) summation as in Fig. 2(a), it is not clear if the earthquake catalogue is complete such that the long-term tectonic loading is adequately represented. Stresses, in turn, might vary at all length scales such that the

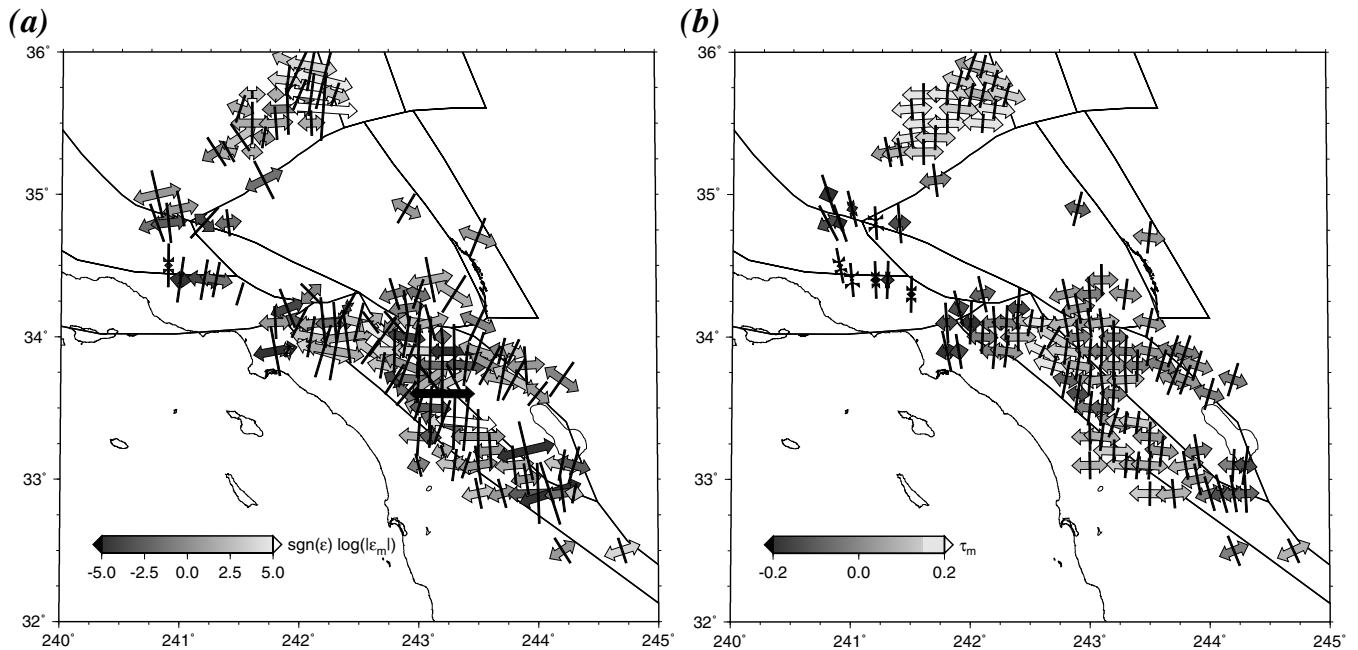


Figure 2. Pre-Landers interseismic deformation based on the Hardebeck & Shearer (2002) catalogue from 1981 to 1992. (a) Binned and summed moment tensors on a $0.1^\circ \times 0.1^\circ$ grid (every other data point shown) interpreted as strain rate $\dot{\epsilon}$. We show the largest, $\dot{\epsilon}_1^h$ (arrows), and smallest, $\dot{\epsilon}_2^h$ (sticks), eigenvectors of the horizontal components of $\dot{\epsilon}$. Shading of the extensional vectors scales with the mean horizontal strain rate, $\dot{\epsilon}_m = (\dot{\epsilon}_1^h + \dot{\epsilon}_2^h)/2$, positive values indicating extension. Stick length and $\dot{\epsilon}_m$ scale with the log of the cumulative moment (arbitrary units). (b) Horizontal stresses from a smoothed, Michael (1984)-type inversion on a $0.1^\circ \times 0.1^\circ$ grid. In analogy with (a), we show τ_1^h (arrows) and τ_2^h (sticks) for the horizontal components of τ and the mean stress τ_m as shading. Inversion results for τ are normalized such that the maximum overall shear stress is $\tau_1 - \tau_3 = 1$; sticks and colour bar have a linear scale. Block geometry (thick lines) and Landers surface rupture (thin lines) are indicated together with shorelines in the background.

inherent or explicit smoothing of both the stress inversions and the moment summation might have no relevance for the loading state close to the fault. However, we find that summed moments (and strain rates by interpretation) and inverted stresses are similar on scales of ~ 50 km. The mean, absolute angular misfit, $\langle |\Delta\alpha| \rangle$, between the $\dot{\epsilon}_1^h$ and τ_1^h tensional axes in Figs 2(a) and (b) is $\approx 7.6^\circ$ based on the 0.1° bins shown. The exploration of the scale dependence of the match between stress inversion and moment summation results will be the subject of future study (see Sheridan & Ben-Zion 2000).

We will assume that the stress inversion results of Fig. 2(b) are indicative of the present-day, interseismic, and regional stress field in southern California. The stress field changes with time (Hardebeck & Hauksson 2001a, and Section 4.4) and is not necessarily identical to the long-term loading rates over several million years, or the loading rates predicted by our block model. The exploration of such deviations is one of the interesting outcomes of our study. For the inversion used, we have $n_\tau = 224$ locations with stress results, leading to $N_\tau = 1344$ components, of which $\nu_\tau = 4n_\tau$ are independent.

2.3 Block models of crustal strain

Deviations of observed crustal velocities from the long-term, rigid motions between lithospheric plates as described by plate-tectonic models such as NUVEL-1A (DeMets *et al.* 1994) indicate intraplate strain accumulation (e.g. Stein 1993; Gordon 2000). The non-rigid velocities on each plate are given by the difference between geological time-scale velocities, v_p , as determined by the Euler poles of the plate motion model, and the geodetic velocities, in our case v_{GPS} . These surface velocities can be described by a number of approaches, as reviewed by Pollitz (2003), who also gives an alternative

description. One end-member strategy consists of the subdivision of the ~ 14 large tectonic plates into smaller parts which move with respect to each other without accounting for strain accumulation at the boundaries (e.g. Drewes 1998). Using this method, much of the velocity field can be explained regionally, such as by introducing an Aegean subdivision to the Anatolian microplate (McClusky *et al.* 2000). The other end-member case is to treat the whole lithosphere as viscously deforming (e.g. England & Molnar 1997). For this approach, strain localization in fault systems is usually approximated by smooth crustal velocity gradients across the whole plate boundary (e.g. Flesch *et al.* 2000; Kreemer *et al.* 2003).

Bourne *et al.*'s (1998) work is an example of a study that falls between these two descriptions of continental tectonics and explores the downward continuation of surface velocities. The authors argue that the relative motions between crustal blocks can be well explained by smooth basal velocity gradients driving a system without significant interseismic strain accumulation in the brittle–elastic part of the lithosphere. Bourne *et al.* consequently average over the velocity gradients that can be detected within individual blocks. Here, however, we are concerned with the detailed strain partitioning of the southern California plate boundary region, and want to take the interseismic deformation into account when associating velocities with slip rates on various segments of the fault system. Hence, we include *a priori* information about strain localization at known geological structures and steep velocity gradients across faults (*cf.* the discussion in Spakman & Nyst 2002). For simplicity, we follow the block modelling (or ‘backslip’) method of Savage & Burford (1973). In this model, interseismic crustal deformation is solely generated by faults that are locked down to an aseismic depth. Plates move at the long-term rates in the far field away from the fault and underneath the locking depth, d_1 , in the aseismic part of the crust

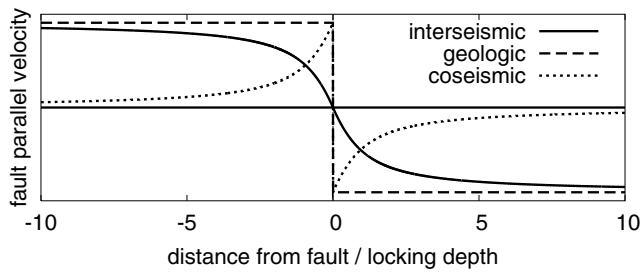


Figure 3. Illustration of the Savage & Burford (1973) block modelling method. The interseismic velocities across a plate-boundary fault can be explained by subtracting the coseismic slip rate (realized during the eventual rupture of the locked fault) from the geological, stepwise velocities. Coseismic slip was determined from an elastic half-space, rectangular, ‘infinite’-length dislocation solution for constant slip (Okada 1992).

and asthenosphere. This implies a transition from localized slip to smooth flow at depths greater than d_1 .

As illustrated in Fig. 3, the interseismically observed velocity field at the surface, $\mathbf{v}_{\text{inter}}$, near the plate boundary, or fault, can then be approximated using a fault model and appropriate \mathbf{v}_p as

$$\mathbf{v}_{\text{inter}} = \mathbf{v}_p - \mathbf{v}_{\text{co}}. \quad (1)$$

The deformation part of the velocity field, $-\mathbf{v}_{\text{co}}$, can be estimated from the displacements that correspond to the earthquake on the fault that would eventually release the strain accumulated during the locked phase. \mathbf{v}_{co} therefore depends on \mathbf{v}_p and the fault geometry, since the average slip rate \mathbf{u} of the fault is given by the relative motion of the neighbouring plates or blocks. $-\mathbf{v}_{\text{co}}$ is responsible for the continuous build-up of elastic strain during the locked part of the earthquake cycle. We will assume that \mathbf{v}_{GPS} is identical to $\mathbf{v}_{\text{inter}}$ everywhere, and that the current interseismic velocities are representative of the long-term behaviour. For very long faults, the shape of the decay of fault-parallel displacement along a profile perpendicular to the fault is only dependent on the fault locking depth d_1 .

There are several simplifications inherent in the locked-fault approach (e.g. Pollitz 2003). Most importantly, any time dependence of the interseismic deformation field is neglected. This could be caused by the faults’ varying proximity to failure in a periodic failure scenario, and by viscoelastic relaxation following large earthquakes (Savage 1990). Following Savage & Lisowski (1998), we can estimate that viscous-relaxation broadening of the velocity gradient across the fault can be expected for normalized Maxwell times of $\eta/(2\mu T) \lesssim 0.2$. Here η , μ , and T denote sublithospheric viscosity, shear modulus, and earthquake cycle time, respectively. This broadening would be interpreted as a large d_1 in our half-space model. Assuming $\mu = 3 \times 10^{10}$ Pa and $T \sim 500$ yr, η should thus be larger than $\eta_c \sim 2 \times 10^{20}$ Pa s for no viscous effects. Viscosities lower than η_c have been reported for the crust (e.g. Kaufman & Royden 1994; Deng *et al.* 1998; Pollitz *et al.* 2001), leading us to expect significant viscoelastic effects (*cf.* McClusky *et al.* 2001). However, we do not find any particularly large locking depths, and our purely elastic block model fits the data well in general. This indicates that post-seismic effects on the GPS measurements might be small regionally on timescales of decades if obvious transients close to large earthquakes such as Landers are excluded (Bennett *et al.* 1996; Meade *et al.* 2002a). However, fault segments that show slow apparent slip in the half-space model (such as the San Andreas SBM segment, see Section 3.1) may alternatively be interpreted as being late in the seismic cycle (Savage & Lisowski 1998).

Savage & Burford’s (1973) backslip method has been used by, for example, Bennett *et al.* (1996) to model GPS velocities and invert for fault slip rates in California. An extension of this approach, in which one solves for individual Euler vectors for each block, was applied to the eastern California shear zone by McClusky *et al.* (2001) and to the Marmara sea by Meade *et al.* (2002b). More recently, Meade *et al.* (2002a) developed an improved block modelling procedure and studied southern California. Smith & Sandwell (2003) used an analogous spectral method to constrain locking depths from GPS data along the SAF. Our approach of velocity modelling follows Meade *et al.* (2002a); the discussion will therefore be brief, and the extension to stresses is straightforward.

2.3.1 Geodetic velocities

We subdivide the study region into crustal blocks on the surface of a sphere. The long-term motion \mathbf{v}_p^i of each micro-plate or block i at location $\mathbf{r} = (x, y, z)$ in a Cartesian system can be described by a block motion (Euler) vector $\boldsymbol{\omega}^i = (\omega_x^i, \omega_y^i, \omega_z^i)$, with

$$\mathbf{v}_p^i = \boldsymbol{\omega}^i \times \mathbf{r}. \quad (2)$$

If we write the Cartesian representation of the two-component geographic ($v_{\text{north}}, v_{\text{east}}, v_{\text{up}} = 0$) GPS velocities, \mathbf{v}_p , as a $N_{\text{GPS}} = 3 n_{\text{GPS}}$ -dimensional vector for n_{GPS} sites, we can set up an inverse problem for rigid-block motions, $\boldsymbol{\omega}_r$, as

$$\mathbf{A}\boldsymbol{\omega}_r = \mathbf{v}_p, \quad (3)$$

where \mathbf{A} is $N_{\text{GPS}} \times 3n_b$ and holds the coordinates of each observation j , \mathbf{r}_j , and $\boldsymbol{\omega}_r$ is $M = 3n_b$ -dimensional with n_b denoting the number of blocks. In our case, $n_b = 12$, with $M = 36$ free parameters for the inversion.

For a locked fault between blocks i and j , we can calculate the additional contribution of deformation to $\mathbf{v}_{\text{inter}}$ by adding $-\mathbf{v}_{\text{co}}$, where the slip for \mathbf{v}_{co} is determined from the relative motion between blocks i and j at \mathbf{r} . Eq. (3) can be augmented such that

$$\mathbf{K}\boldsymbol{\omega} = (\mathbf{A} - \mathbf{DGF})\boldsymbol{\omega} = \mathbf{v}_{\text{inter}} \approx \mathbf{v}_{\text{GPS}}, \quad (4)$$

where \mathbf{D} relates fault-local slip to global displacements (or velocities); \mathbf{D} is $N_{\text{GPS}} \times 2n_{\text{fault}}$, where n_{fault} is the number of faults. The factor 2 in the number of rows arises from the allowed fault motions: strike- and normal slip for vertical faults, and strike-slip and dip motion for non-vertical faults. The long-term block motion $\boldsymbol{\omega}$ in (4) is different from $\boldsymbol{\omega}_r$ in (3) in that it is derived including the effect of strain accumulation along block boundaries.

Algorithms to calculate dislocation solutions in a spherical earth are available but numerically expensive (e.g. Nostro *et al.* 1999). Since deviations between flat and spherical approaches are small for displacements in the near field (few fault lengths), we therefore approximate \mathbf{D} by using rectangular Okada (1992) dislocation patches for an elastic half-space. We strive to minimize the effect of curvature in our half-space representation by evaluating displacements in a fault-local oblique Mercator system (Meade *et al.* 2002a). \mathbf{D} includes the conversion to Cartesian velocities and depends on fault geometry; so does \mathbf{G} , which relates global relative motion to fault-local slip. \mathbf{F} depends only on the location of the fault mid-point and converts block motions to global relative displacements in the half-space.

We solve eq. (4) for ω in a least-squares sense by weighting the rows of \mathbf{K} and entries of \mathbf{v}_{GPS} with the inverse of the data uncertainties; then we perform a singular value decomposition (SVD):

$$\mathbf{K} = \mathbf{U} \text{diag}(s_i) \mathbf{V}^T, \quad \text{with} \quad \mathbf{U}^T \mathbf{U} = \mathbf{V}^T \mathbf{V} = \mathbf{1}, \quad (5)$$

where $\mathbf{1}$ is the unity matrix. The best-fit solution is given by

$$\omega = \mathbf{V} \text{diag}(1/s_i) \mathbf{U}^T \mathbf{v}_{\text{GPS}} \quad (6)$$

(e.g. Press *et al.* 1993, p. 676f). The M singular values (SV), s_i , and eigenfunctions in \mathbf{V} can be used to calculate the covariance

$$\mathbf{C} = C_{ij} = \sum_{k=1}^M \left(\frac{V_{ik} V_{jk}}{s_k^2} \right) \quad (7)$$

between ω_i and ω_j ; the uncertainty in solution parameter ω_i , σ_{ω_i} , is then given by $\sqrt{C_{ii}}$.

2.3.2 Stress

For a homogeneous, linear elastic medium in our idealized loading model, the elastic strains of the superimposed dislocation solutions correspond to loading stresses. Our goal is to compare these predicted stressing rates with the stress model we derived from focal mechanisms, ignoring for the moment any background stress (e.g. from topography and material heterogeneities) to which they are added. We will show that the stressing rates from the block model align with the results from the focal mechanism inversion. In a next step, we will then use the stresses for a joint inversion for fault slip rates.

If we expand the N_{GPS} data vector $\mathbf{y} = \mathbf{v}_{\text{GPS}}$ by the $N_\tau = 6n_\tau$ stress components of $\boldsymbol{\tau}$ we can write

$$\hat{\mathbf{K}} \omega = \begin{pmatrix} \mathbf{A} & -\mathbf{DGF} \\ & -\mathbf{IGF} \end{pmatrix} \omega = \mathbf{y} = \begin{pmatrix} \mathbf{v}_{\text{GPS}} \\ \frac{\beta}{3} \boldsymbol{\tau} \end{pmatrix}, \quad (8)$$

where $\beta/3$ is the weight of the $6n_\tau$ stress entries in the \mathbf{y} data vector compared with $2n_{\text{GPS}}$ velocity data. $\mathbf{A} - \mathbf{DGF}$ fills the first N_{GPS} rows of $\hat{\mathbf{K}}$, and \mathbf{I} relates fault-local slip to global stress in analogy with \mathbf{D} . (There is no stress analogue to \mathbf{A} since no deformation occurs between blocks without fault-related locking.) Stresses are evaluated at a constant depth of 5 km. Results for stress model misfit do not depend strongly on this choice for depths shallower than 5 km, but the misfit increases monotonically for greater depths. Below, we will sometimes lump together GPS velocity observations and stresses from focal mechanism inversions as ‘data’; we recognize that both \mathbf{v}_{GPS} and particularly $\boldsymbol{\tau}$ are models and not primary data.

We define the total, χ^2 , and reduced, $\hat{\chi}^2$, misfits as

$$\chi^2 = \frac{\chi_{\mathbf{v}}^2 + \beta \chi_{\boldsymbol{\tau}}^2}{1 + \beta}, \quad \hat{\chi}^2 = \frac{\chi^2}{\nu_{\mathbf{v}} + \nu_{\boldsymbol{\tau}} - M - 1}, \quad (9)$$

and the variance reduction, VR , as

$$VR = 1 - \left(\frac{\chi^2}{|\mathbf{y}|^2} \right)^{1/2}, \quad (10)$$

with velocity, $\chi_{\mathbf{v}}^2$, and stress misfit, $\chi_{\boldsymbol{\tau}}^2$, given as

$$\chi_{\mathbf{v}}^2 = \sum_{i=1}^{N_{\text{GPS}}} \frac{(y_{\text{mod}}^i - y^i)^2}{(\sigma_{\text{GPS}}^i)^2}, \quad \chi_{\boldsymbol{\tau}}^2 = \sum_{i=N_{\text{GPS}}+1}^{N_{\text{GPS}}+N_\tau} \frac{(y_{\text{mod}}^i - y^i)^2}{(\sigma_{\boldsymbol{\tau}}^i)^2}. \quad (11)$$

Here, σ^i denotes the uncertainties in each quantity, and \mathbf{y}_{mod} is the approximation to \mathbf{y} from least squares. For VR , $|\mathbf{y}|^2$ is obtained by analogy with eq. (11), and χ^2 for $\mathbf{y}_{\text{mod}} = \mathbf{0}$.

2.3.3 Solution and damping procedure

If we knew the absolute values of $\boldsymbol{\tau}$ and the material properties of the study region, we could solve eq. (8) by least-squares like eq. (4). Since the amplitude of stress is not constrained, however, we proceed as follows: solve for block motions using eq. (4); scale stress ‘data’ to the amplitudes predicted initially by the block model; solve eq. (8); rescale to the new slip-model; and iterate until convergence is achieved. For $\beta = 1$, this procedure typically leads to a reduction in the χ^2 misfit of the stresses by a factor of 2 and a reduction in stress amplitudes of ~ 10 per cent when compared with the scaled stresses predicted from eq. (4). We have conducted additional Levenberg–Marquardt and Monte Carlo inversions of eq. (8) to test if our simple iteration scheme pulls the solution to small-amplitude, low-magnitude local misfit minima. The best models achieved with the non-linear methods were very similar to the iterated models, however, and we will only show results from the iteration approach below.

We allow for strike and normal motion on faults but recognize that motion on faults in southern California should be predominantly strike-slip. We therefore introduce a damping vector $\boldsymbol{\gamma}$ with $2n_{\text{fault}}$ components,

$$\boldsymbol{\gamma} = (0, \gamma, 0, \gamma, \dots, 0, \gamma), \quad (12)$$

where values for the strike and normal motion alternate. We also found it advantageous to damp the ω solution by a scaling factor α towards the rigid-block motion, ω_r , as found by (3). Eq. (8) can then be modified so that

$$\hat{\mathbf{K}} \omega = \begin{pmatrix} \mathbf{A} & -\mathbf{DGF} \\ & -\mathbf{IGF} \\ & \boldsymbol{\gamma} \mathbf{GF} \\ & \alpha \mathbf{1} \end{pmatrix} \omega = \mathbf{y} = \begin{pmatrix} \mathbf{v}_{\text{GPS}} \\ \frac{\beta}{3} \boldsymbol{\tau} \\ \mathbf{0} \\ \alpha \omega_r \end{pmatrix}, \quad (13)$$

where $\mathbf{1}$ is a $3n_b \times 3n_b$ unity matrix. We can then tune the solution from no ($\gamma = 0$) to strong normal slip damping ($\gamma \gg 1$), and from the unconstrained deformation ($\alpha = 0$) to the rigid block ω ($\alpha \gg 1$). We select $\gamma = 0.1$ from evaluation of the trade-off between $\chi_{\mathbf{v}}^2$ and the RMS normal fault slip motion for $\beta = 0$. This choice results in a reduction of normal fault motion by ~ 30 per cent and a slight increase of $\chi_{\mathbf{v}}^2$ by ~ 2 per cent. Our pick of $\alpha = 0.05$ is guided by the trade-off between $\chi_{\mathbf{v}}^2$ and the norm of the ω uncertainties, σ_{ω} , as computed from (7). For $\alpha = 0.05$, $|\sigma_{\omega}|$ is decreased by 67 per cent while the $\chi_{\mathbf{v}}^2$ misfit is only increased by ~ 1 per cent from the $\alpha = 0$, $\gamma = 0.1$ solution.

We found that all solutions were stable with respect to the relative block motions as mapped into the fault slip rates when the damping scheme was modified in terms of α , or if small singular values were eliminated for $\alpha = 0$. However, damped models have smaller formal uncertainties in the Euler vectors and smaller covariances. Fig. 4(a) shows \mathbf{C} and σ_{ω_i} for a velocity-only inversion and $\alpha = 0$. There are large uncertainties in ω and off-diagonal entries in \mathbf{C} if we do not damp the solution, indicating significant trade-offs between individual ω^i Euler vectors. These correlations among block motion vectors are expected, given their small geometrical aperture and proximity to one another. The choice of $\alpha = 0.05$ for damping towards ω_r suppresses most off-diagonal entries in \mathbf{C} and leads to smaller uncertainties (Fig. 4b). Our correlation matrix is biased in the sense that not only does it reflect the propagation of velocity measurement errors to ω estimates, but \mathbf{C} also depends on the damping parameters. Decreasing formal uncertainties therefore do

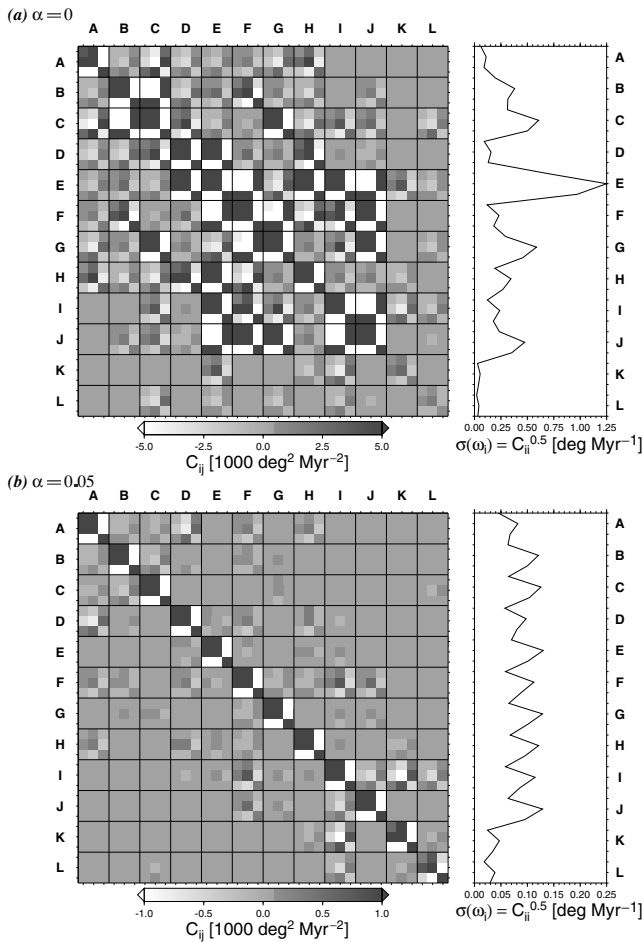


Figure 4. Covariance matrix \mathbf{C} (left subplots) for the $n_b \times 3 = (12 \times 3)$ -dimensional block motion vector, ω , for a GPS-only inversion ($\beta = 0$, $\gamma = 0.1$, see Sections 2.3.2 and 2.3.3) using no damping (part a, $\alpha = 0$) and some damping of the solution towards ω_r (part b, $\alpha = 0.05$). Axes are labelled with the block codes as in Fig. 1. Right subplots show $\sqrt{C_{ii}}$ (1σ uncertainties for ω_i) versus block code. Note that the scale changes by a factor of 5 between a and b.

not necessarily mean a better solution, but we prefer the damped inversion as it has a smaller model norm.

We have experimented with a range of damping schemes and noticed that the solution for ω is not as well constrained as the fault slip rates. The inversion for relative block motions is independent of the velocity reference frame, and any closed circuit across block boundaries adds up to zero relative Euler vectors (Meade *et al.* 2002b). However, we found that there are differences in the predicted ω models, depending on whether we damp towards ω_r using $\alpha \neq 0$, or if we damp by eliminating small SVs in (6). When we compare the differences in the predicted Euler vectors for these damping schemes, we find small residual rotations with Euler poles mostly within the blocks. For instance, the $\alpha \neq 0$ model has block A rotate counter-clockwise and block F clockwise with respect to the SVD damped solution. These relative rotations correspond to faster left-lateral slip rates of $\sim 3 \text{ mm yr}^{-1}$ on the Garlock fault for α damping compared with SV only, higher than the GPS uncertainties. We also found that slightly different predictions for ω arise for SV elimination depending on the initial reference-frame correction for the GPS velocities. We therefore chose to damp our solution by $\alpha = 0.05$ towards the rigid-block motion, as noted above, for this

damping method results were independent of the GPS reference frame.

2.3.4 Block geometry

We use a block geometry that is greatly simplified with respect to mapped faults, while still containing the major fault strands of the San Andreas system, specifically the San Jacinto and Elsinore segments (Figs 1 and 2). Our choice of fault locations was primarily guided by mapped surface traces along the major strands of the SAF system (after Jennings 1975). All fault segments are vertical (90° dip). We experimented with low-angle thrust faults in the Transverse Ranges (results not shown) but model misfit was only slightly improved, so we prefer to discuss results mainly from the simpler model.

The fault segments as depicted in Fig. 1 were subdivided into numerous rectangular dislocation patches for the inversion procedure. The typical along-strike length and down-dip width of each patch were $\sim 6 \text{ km} \times 15 \text{ km}$; further lateral refinement (or coarsening) did not affect the results significantly. We will mainly use pre-assigned locking depths to each fault segment from seismicity (Hauksson 2000), with typical values of $\sim 15 \text{ km}$ which were held fixed. We explore spatial variations in locking depth in Section 4.2.

We realize that our basic model does not completely capture the geometrical and geological complexity of the plate boundary system in southern California. Our model also suffers from some artefacts due to edge effects. However, we defer a refinement of the fault geometry to subsequent work and discuss the robustness of our results with the help of an example of an alternative geometry in Section 4.5.

3 RESULTS

3.1 GPS-only inversion

Fig. 5 shows residual velocities at each site i , $\Delta \mathbf{v}^i = \mathbf{v}_{\text{GPS}}^i - \mathbf{v}_{\text{mod}}^i$, inverted for block motion vectors given velocity observations ($\beta = 0$) using damping of $\alpha = 0.05$ and $\gamma = 0.1$. The linewidth along faults indicates strike-slip (Fig. 5a) and normal slip rates (Fig. 5b) (*cf.* Meade *et al.* 2002a). The mean velocity misfit of this model, $\langle |\Delta \mathbf{v}| \rangle$, is $\approx 2.1 \text{ mm yr}^{-1}$ (1.4 mm yr^{-1} component-wise). This value is comparable to the uncertainty in the GPS data, with 56 and 90 per cent of our residuals smaller than 2 mm yr^{-1} and 4 mm yr^{-1} , respectively. Some of the larger deviations could be reduced by a modified fault geometry or further editing of outlier data. If we use all data from SCEC3, the mean misfit is increased to $\langle |\Delta \mathbf{v}| \rangle \approx 2.4 \text{ mm yr}^{-1}$.

For the model in Fig. 5, $\chi^2 = \chi_v^2 = 3082$ ($VR = 91.5$ per cent, $\hat{\chi}^2 = 3.0$), which is substantially smaller than the misfit we obtain for rigid-block motions without any strain accumulation, namely $\chi_v^2 = 6267$ ($\hat{\chi}_v^2 = 6.1$). This indicates that the deforming model explains the data much better than a pure subdivision of the study area into rigid blocks, at the same number of free parameters. Using all SCEC3 data for the deforming model, we find $\hat{\chi}^2 = 3.8$.

We list the Euler vectors, ω , and the best-fit rigid ω_r solution for all blocks in the Appendix (Tables A1 and A2). Taking the relative motion between blocks K and L as a regional approximation to the plate-tectonic motion of the Pacific plate with respect to stable North America, we find that the positive $|\omega|$ Euler poles from our inversion, ω , lie typically to the northwest of that from NUVEL1-A (DeMets *et al.* 1994), $\omega^{\text{PAC-NAM}}$, and have larger amplitudes

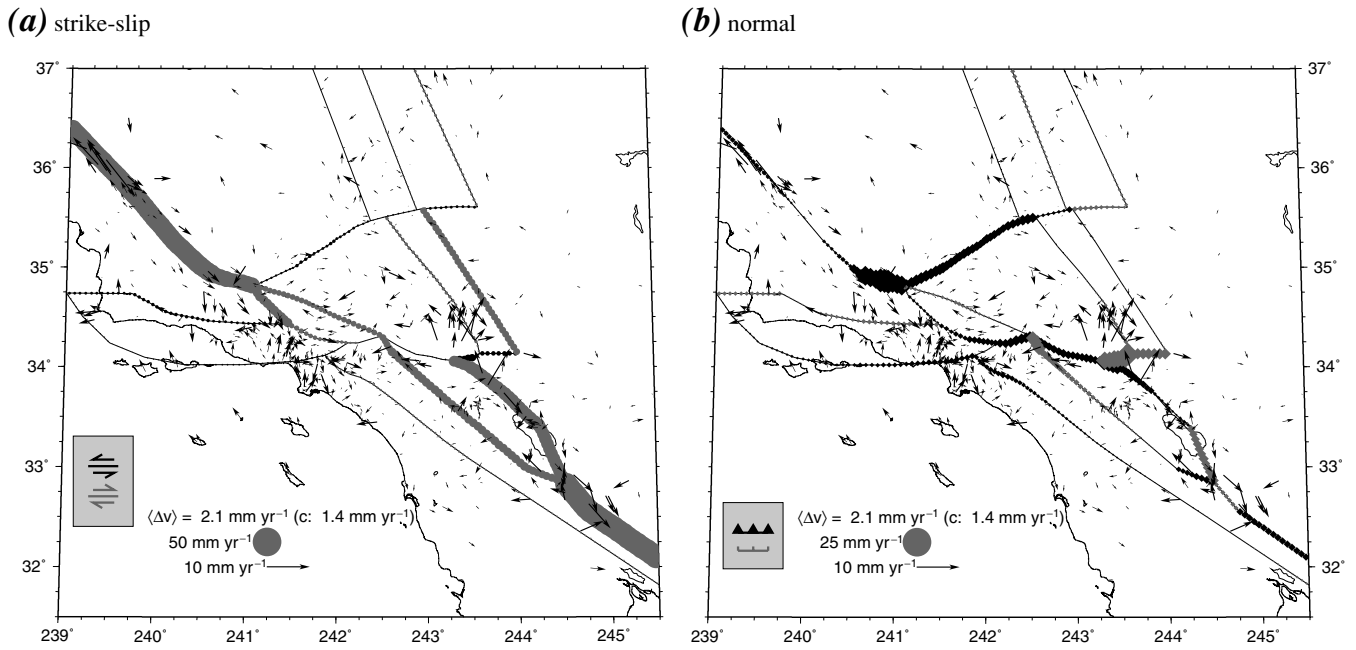


Figure 5. Residual GPS velocities Δv^i and predicted fault slip rates for an inversion of v_{GPS} only, $\beta = 0$. (Note that the velocity vector scale is different from in Fig. 1.) Shaded circles are plotted at the centre of each dislocation patch and scale with the slip rate. Dark and light shading indicates left-lateral and right-lateral motion for plot (a) and closing and opening motion for plot (b), respectively. The scale for slip rates [different for (a) and (b)] and residual velocities is indicated along with the mean residual velocity vector length, $\langle |\Delta v^i| \rangle$, and the component-wise mean misfit (in brackets).

Table 1. Average fault slip rate, u , in strike ($u > 0$: right-lateral, $u < 0$: left-lateral) and normal ($u > 0$: opening, $u < 0$: shortening) directions for fault segments numbered as in Fig. 1 for GPS-only inversion ($\beta = 0$, Fig. 5) and joint inversion ($\beta = 1$, Fig. 7). Averaging is performed over all subdivisions of the main, straight segments shown in Fig. 1. Indicated \pm ranges are conservative estimates of systematic uncertainties; they are the standard deviations from the mean obtained by randomizing ω using σ_ω from (7). ‘Palaeoseismology’ slip rates include estimates from geomorphology and are rough indications only (see Section 4.3). References listed by segment code: (1) Thomas & Rockwell (1996), \sim half of total in this region; (2) Magistrale & Rockwell (1996) and Vaughan *et al.* (1999); (3) Sharp (1981), Prentice *et al.* (1986), Rockwell *et al.* (1990) and Dorsey (2002); (4) van der Woerd *et al.* (2001); (5) Harden & Matti (1989); (6) Santa Monica system: left-lateral: Treiman (1994), Dolan *et al.* (1995) and Hitchcock *et al.* (2003); thrust: Crook *et al.* (1987), Dolan *et al.* (2000) and McGill (1989). San Cayetano, Cucamonga, and Sierra Madre faults show thrust rates of 1–8 mm yr^{-1} (Rockwell 1988), 3–5 mm yr^{-1} (Walls *et al.* 1997), and 1–3 mm yr^{-1} (Walls *et al.* 1997), respectively; (7) Weldon & Sieh (1985); (8) and (9) Dokka & Travis (1990); (10) Sieh & Jahns (1984); (11) McGill & Sieh (1993); (12) Combination of Deep springs: 1 mm yr^{-1} normal (Lee *et al.* 2000; Schroeder *et al.* 2002), Owens Valley: 1–3 mm yr^{-1} right-lateral (Beanland & Clark 1993; Lee *et al.* 2000; Dixon *et al.* 2003), \sim 1 mm yr^{-1} normal (Beanland & Clark 1993).

Code no. Fig. 1	fault segment or region	$\beta = 0$ inversion		$\beta = 1$ inversion		Palaeoseismology strike-slip rate unless otherwise indicated [mm yr^{-1}]
		strike-slip rate [mm yr^{-1}]	normal rate [mm yr^{-1}]	strike-slip rate [mm yr^{-1}]	normal rate [mm yr^{-1}]	
1	Imperial	39.5 ± 7	4.4 ± 10	38.5 ± 5	2.3 ± 8	15 ... 20 (\sim half of total)
2	Elsinore	3.7 ± 7	-2.3 ± 10	3.7 ± 6	0.8 ± 8	4 ... 6
3	San Jacinto	15.3 ± 11	3.1 ± 15	14.5 ± 9	1.9 ± 12	\sim 15
4	San Andreas Indio	23.0 ± 8	-2.7 ± 12	22.9 ± 8	-3.5 ± 11	23.3 ± 3.5
5	San Andreas SBM	-2.3 ± 15	-7.5 ± 13	0.9 ± 12	-11.0 ± 10	14 ... 35
6	Transverse	-2.5 ± 11	-3.9 ± 10	-2.4 ± 11	-2.0 ± 9	-1 and \sim 1 thrust
7	San Andreas Mojave	9.4 ± 13	3.3 ± 15	15.7 ± 12	-0.3 ± 13	24 ± 3.5
8	East Cal Shear Zone West	5.7 ± 11	0.3 ± 16	4.5 ± 9	2.0 ± 14	6 ... 12 for both
9	East Cal Shear Zone East	12.4 ± 8	0.7 ± 13	9.4 ± 8	-0.2 ± 12	-
10	San Andreas Carrizo	33.1 ± 9	-2.6 ± 12	26.8 ± 8	-2.6 ± 11	33.9 ± 2.9
11	Garlock	-4.8 ± 14	-8.7 ± 9	-3.1 ± 10	0.6 ± 7	-5 ... -7
12	Basin and Range West	1.0 ± 10	-0.3 ± 14	6.8 ± 8	5.3 ± 12	6 ... 8 and \sim 2 normal for both
13	Basin and Range East	4.6 ± 8	0.9 ± 13	4.1 ± 8	2.2 ± 13	

(Table A2). Some selected long-term slip rates derived from ω are listed in the left part of Table 1 and sorted by fault segment codes as shown in Fig. 1. These uncertainties are based on σ_ω from (7). They were obtained by randomizing the ω solution, and the quoted \pm ranges in Table 1 indicate the standard deviation from the mean. We think that these, rather high, uncertainties are a conservative es-

timate of the systematic errors in the solution procedure for ω . The uncertainties in the fault slip rates based solely on the GPS input data are much lower, of the order of a few mm yr^{-1} . If we damp the solution further using SV elimination, if we base our block model on the complete SCEC3 data set, or if interpolated velocities as in Fig. 1 are used, fault slip rates are similar to the solution shown in

Table 1 to within $\pm \sim 2 \text{ mm yr}^{-1}$. This indicates that slip rates can be robustly determined.

The major strike-slip motion of the plate boundary in Fig. 5 is partitioned, from south to north and west to east, between Elsinore, San Jacinto, and San Andreas Indio, to Tejon Pass, SAF Mojave, and Eastern Cal Shear Zone, to San Andreas Carrizo, and Basin and Range. Based on the inversion of GPS data only (Fig. 5), we find that the slip in the southern portion of the region is primarily divided between the Indio segment of the SAF and the SJF, with more slip on the SAF ($\sim 23 \text{ mm yr}^{-1}$ compared with $\sim 15 \text{ mm yr}^{-1}$). Further north, the ECSZ (fault nos 8 and 9 in Fig. 1) takes up about $\sim 18 \text{ mm yr}^{-1}$ of right-lateral slip, with the rest distributed on the western faults, including the Mojave segment of the SAF. The SAF fault segment south of the San Bernardino mountains (no. 5 in Fig. 1) takes up a small amount of left-lateral motion ($\sim 2 \text{ mm yr}^{-1}$), with large formal uncertainties, so that we cannot distinguish it from not slipping at all. Other segments with left-lateral motion are found in the Transverse ranges and on the Garlock fault. If we constrain fault segments with poor data coverage such as no. 5 at SBM to slip right-laterally (results not shown), the surrounding fault slip rates are not modified significantly from the solution shown in Fig. 1. Fault-normal motion is characterized by thrust features in the San Fernando valley and Tejon Pass regions that are broadly consistent with geological observations. We also predict shortening across the Garlock fault, but this feature is not found in the joint inversion (see below).

Fig. 6(a) shows the horizontal part of the predicted stressing rates from the GPS-only inversion compared with the stress as found from the focal mechanisms. The block model produces the general north-south orientation of compressive stresses as derived from

seismicity, and also captures some of the regional variations. The mean, weighted misfit of the major horizontal stress axis is $\sim 9.4^\circ$, which is within the uncertainties of the stress inversion. This result implies that interseismic loading and seismicity appear to be correlated over the lengthscales and timescales we have studied in our model. Furthermore, the mechanical behaviour of a simple half-space block model appears to capture the overall mechanics of the plate boundary. For a homogeneous elastic medium, the strain rates from GPS velocities correspond to tectonic loading stresses, which appear to be aligned with the stress from seismicity for the study region. We use this finding to proceed with a joint inversion, in which we assume that this alignment holds everywhere.

3.2 Joint inversion

Fig. 7 and the middle part of Table 1 show how slip rates are modified when we additionally use the stress model as input for our inversion by setting the weight to $\beta = 1$. The misfit to the GPS velocities is slightly larger for this joint model, with $\langle \Delta \mathbf{v} \rangle \approx 2.3 \text{ mm yr}^{-1}$ ($\chi_v^2 = 3666$, compared with the $\beta = 0$ result ($\langle \Delta \mathbf{v} \rangle \approx 2.1$, $\chi_v^2 = 3082$). The predicted slip rates on the major fault segments are similar for the models of Figs 5 and 7 in general. However, slip in the ECSZ and the Basin and Range is repartitioned, and the SAF Mojave segment moves faster for $\beta = 1$ (Table 1). The basic slip partitioning between the SAF, SJF and ECSZ remains the same as for the $\beta = 0$ model. The Indio SAF still accommodates more slip than the SJF. The ECSZ takes up somewhat less total slip in the $\beta = 1$ model, so again slip must be transferred from the Indio SAF to the Mojave SAF. The distribution of slip in the SBM region is different from in the

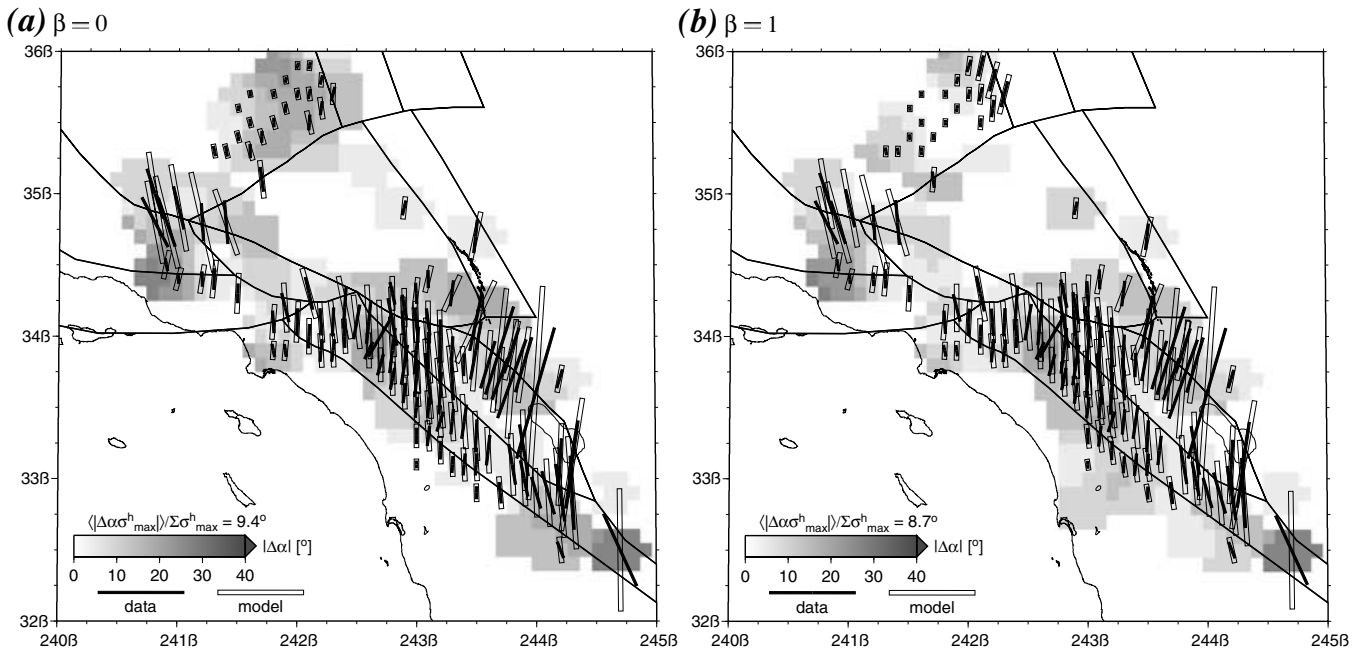
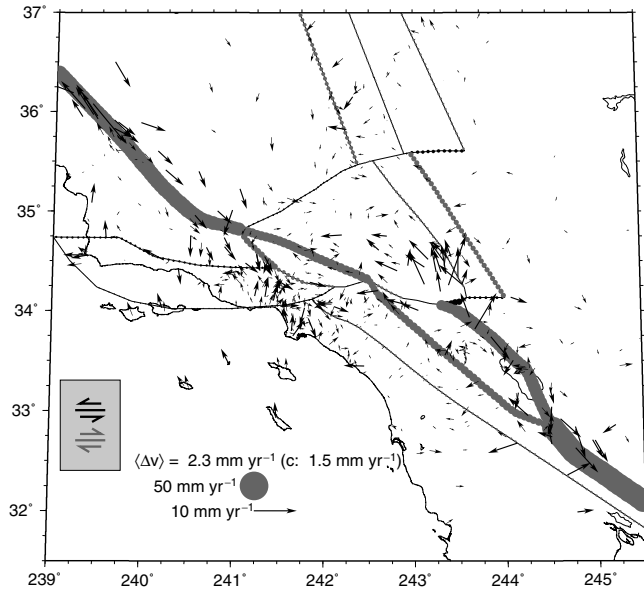
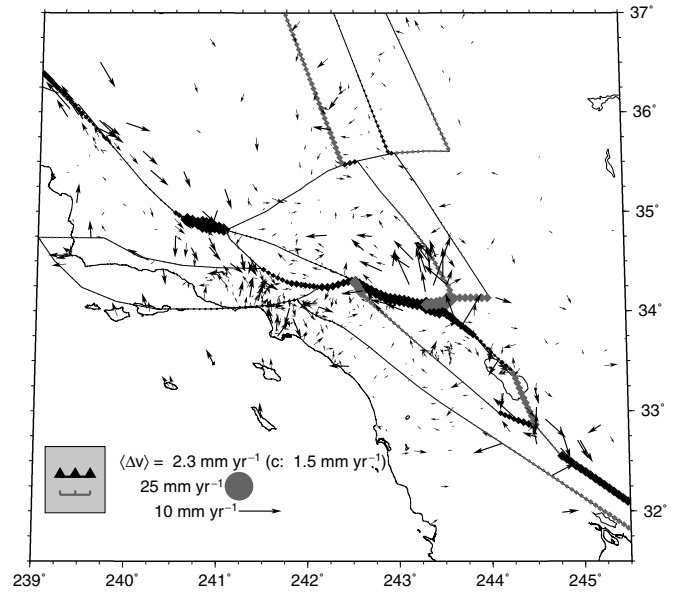


Figure 6. Pre-Landers horizontal stress components as found from focal mechanism inversion ('data'-labelled sticks, as in Fig. 2(b) but scaled to model amplitudes) and predicted by the block model (open bars) for $\beta = 0$ (part a, τ not weighted in inversion) and $\beta = 1$ (part b). Stick orientation shows the major compressive stress axes, $\mathbf{e}_{\tau_2^h}$, and length scales with the maximum horizontal shear stress. For visualization purposes, we only show every third stress data point. Background shading shows the absolute angular deviation, $|\Delta\alpha|$, between the model and observed $\mathbf{e}_{\tau_2^h}$ in degrees. The mean weighted deviation, $\langle |\Delta\alpha\sigma_{\max}^h| \rangle / \sum \sigma_{\max}^h$, is given in the legend. This quantity weights the misfit by the maximum horizontal shear stress, σ_{\max}^h , to emphasize the regions with a strong signal; the sum $\sum \sigma_{\max}^h$ is computed over all grid entries. Fine lines denote the fault trace of the Landers 1992 event ($\sim 243.5^\circ\text{E}/34.3^\circ\text{N}$, see Figs 2 and 11).

(a) strike-slip



(b) normal

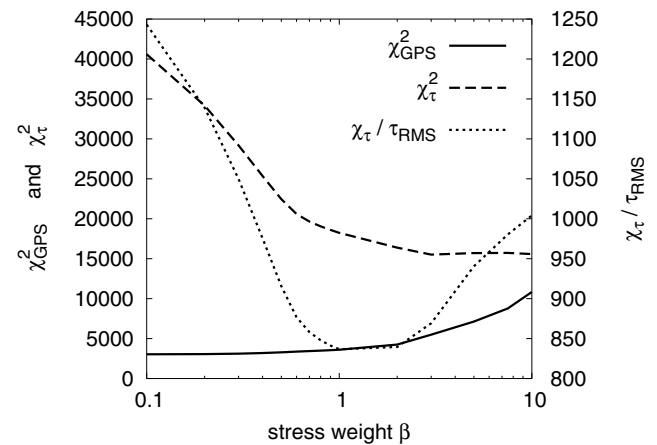

Figure 7. Residual GPS velocities Δv and predicted fault slip rates for a joint inversion of GPS and stress data, $\beta = 1$ (compare with Fig. 5).

$\beta = 0$ model: the SBM segment of the SAF is predicted to move hardly at all for $\beta = 1$.

Variations in slip rates between the $\beta = 0$ and $\beta = 1$ models are more pronounced in the fault-normal direction. The (poorly constrained) shortening we found across the Garlock fault for $\beta = 0$ is now suppressed. Thrust motion is instead placed on the SBM region ($\sim 11 \text{ mm yr}^{-1}$). Other differences include a larger extensional component for the Basin and Range. Including stresses from focal mechanisms in a joint inversion is therefore useful since it leads to better constrained, and more geologically reasonable (we contend), slip rates in regions where there is sparse geodetic coverage (*cf.* Kreemer *et al.* 2003), such as around SBM.

Fig. 6 shows the horizontal part of the predicted stress field in our model, both for the GPS-only inversion (Fig. 6a, $\chi_{\tau}^2 = 42312$) and the $\beta = 1$ joint inversion of Fig. 7 (Fig. 6b, $\chi_{\tau}^2 = 19092$, $\chi^2 = 7523$, $\hat{\chi}^2 = 3.9$). The trade-off between fit to the GPS and stress data is quantified in Fig. 8, which shows χ_{τ}^2 and χ_{τ} normalized by the RMS of the scaled model stresses, $\chi_{\tau}/\tau_{\text{RMS}}$, for various weightings of the stress data, β , at $\alpha = 0.05$ and $\gamma = 0.1$. We see that part of the reduction in the χ_{τ} misfit for stress is accompanied by a decrease in the stress amplitudes. However, between $\beta = 0$ and $\beta \sim 1$ there is a clear improvement in model fit to stresses, while the fit to velocities only deteriorates slightly. This is why we pick $\beta = 1$ for the joint inversion.

The inclusion of the stress model in the inversion for block motion leads to a visually improved model fit to observed stresses in some regions (Sierra Nevada, Tejon Pass, SBM), but to only a minor improvement in the mean weighted angular misfit of the horizontal compressive stress axes (see legends in Fig. 6). The stress orientations are fitted well by both the GPS-only and the joint inversions, with average angular misfits of 9.4° and 8.7° , respectively, compared with the stress observation uncertainty of $\sim 15^{\circ}$. If we use a normalized version of the binned and non-smoothed Kostrov strain rates as depicted in Fig. 2(a) for the inversion instead of the smoothed pre-Landers stresses, the mean angular misfit of this strain model is


Figure 8. Misfit of model velocities, χ_{GPS}^2 , and stresses, χ_{τ}^2 , as well as χ_{τ} normalized by the RMS of the scaled model stresses, $\chi_{\tau}/\tau_{\text{RMS}}$, for various weightings of the stress data, β , at $\alpha = 0.05$ and $\gamma = 0.1$.

($|\Delta\alpha| \approx 11.9^{\circ}$ for $\beta = 1$, a comparable misfit to that in the stress inversion.

4 DISCUSSION

We have shown that a block model of strain accumulation in the southern California plate boundary zone can be well constrained by the GPS data that have become available over the past decade, substantiating earlier findings (Bennett *et al.* 1996; Meade *et al.* 2002a; Smith & Sandwell 2003). Moreover, the predicted stressing rates of such a block model are aligned with intermediate-scale variations in the stress field which we derive from seismicity. Taking those stress inversions into account in a joint inversion for slip rates leads to better constrained rates in regions with poor GPS coverage (*cf.* Kreemer *et al.* 2003). This is an encouraging result, since it is not clear that the various simplifications we have to make for this comparison

(homogeneous elastic parameters, stress from seismicity indicative of regional loading, time independence of interseismic strain accumulation) are justified. This suggests that stress orientations could be used in the future to constrain fault slip in other regions.

We find that stress orientations from our seismicity inversions are well aligned with the predicted stressing rate. There are two possible interpretations of this finding. First, if the Michael (1984)-type seismicity inversion actually finds the stress tensor, then our result means that the compressive stress axis is aligned at 45° to the faults. This also implies that the background stress heterogeneity that is unrelated to the tectonic loading has little detectable signal on the lengthscales considered. The second possibility is that the seismicity inversion detects the stress-rate tensor (Smith & Heaton 2003). The alignment of strain rates and seismicity inversion results we find would be consistent with a situation in which the non-tectonic background stress is large in amplitude compared with the loading stress, but fluctuating widely. In this scenario, seismicity (and stresses derived from it) would be biased by the effect of cumulative loading (Smith & Heaton 2003).

4.1 Slip distribution

The distribution of slip on the southernmost San Andreas system in our joint inversion is broadly consistent with the first of the previously proposed models (Section 1). Our model supports the notion of high slip on the SJF and low slip on the SBM segment of the SAF. The SAF Indio slips at $\sim 23 \text{ mm yr}^{-1}$, faster than the SJF ($\sim 15 \text{ mm yr}^{-1}$); this inferred difference in strain accumulation is in contrast to seismicity rates that are higher on the SJF (e.g. Hauksson 2000). South of the San Bernardino Mountains, the total slip on the Indio SAF and SJF is somewhat larger than expected, $\sim 38 \text{ mm yr}^{-1}$ as opposed to $\sim 35 \text{ mm yr}^{-1}$, perhaps because our fault-model simplifications lead to the concentration of slip on these two faults. North of the SBM, the Mojave segment of the SAF accommodates $9\text{--}16 \text{ mm yr}^{-1}$, while the ECSZ also has $15\text{--}18 \text{ mm yr}^{-1}$ rates. The slip on the Mojave SAF is approximately equivalent to the slip on the SJF for $\beta = 1$, while the slip on the Indio SAF is only slightly higher than the ECSZ slip, meaning that slip is partitioned into a SJF–Mojave line in the west and a Indio–ECSZ line in the east (Figs 5 and 7). Very little slip is transferred between these two systems, resulting in a low ($< 10 \text{ mm yr}^{-1}$) slip on the SMB segment of the SAF, less than in either of the previously proposed models.

4.2 Locking-depth variations

As discussed in Section 2.3, the fault locking depth, d_1 , is the major control on the width of the transition between v_{GPS} and v_p across faults. We typically use locking depths as inferred by hand from the depth of seismicity in the Hauksson (2000) catalogue, but now explore the variation of model misfit as a function of d_1 .

Fig. 9 shows χ^2 misfits versus regionally constant locking (or fault segment) depth. Restricting the inversion to GPS data ($\beta = 0$), we find that there is a broad minimum of χ^2 for locking depths of $\sim 9 \text{ km}$. The best fit for constant d_1 is $\chi_v^2 = 2942$, which compares with $\chi_v^2 = 3082$ for our previous inversions where d_1 varies between faults. This indicates that our assumption that d_1 represents the seismic/aseismic transition is plausible but leads to slightly worse misfits than constant d_1 for $\beta = 0$. Including stresses in the inversion for $\beta = 1$ models leads to similar behaviour for χ_v^2 , while the minimum in χ_τ^2 for both $\beta = 0$ and $\beta = 1$ is smeared out, indicating insufficient resolution of the stress data for locking depths (Fig. 9). For $\beta = 1$, the model with regional variations in d_1 from seismicity

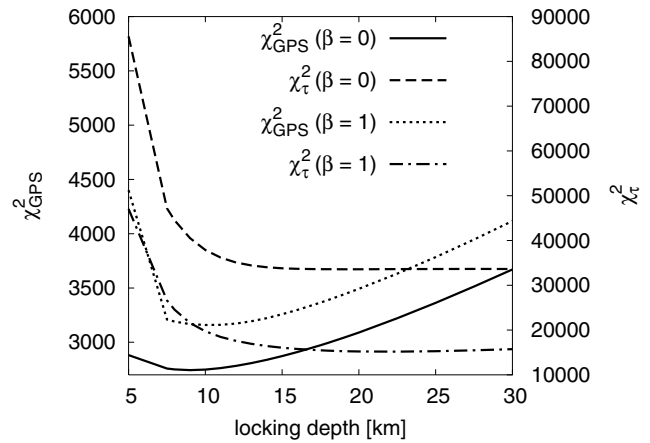


Figure 9. χ^2 misfits for GPS and stress data (eq. 9) for $\beta = 0$ velocity-only, and $\beta = 1$ joint inversion versus global locking depth ($\alpha = 0.05$ and $\gamma = 0.1$).

performs better than that with constant d_1 ($\chi^2 = 7523$ versus $\chi^2 = 8233$), which is why we have used the seismicity-based d_1 for most models.

We have also explored improving the model misfit by inverting for variations in d_1 along faults (Fig. 10). For $\beta = 0$ models, the χ_v^2 could be reduced to ~ 2242 ($\hat{\chi}^2 = 2.2$) by treating d_1 for 50-km-length subdivisions of faults as a free parameter (Fig. 10b). One of the most robust signals for regional variations in d_1 came from the Parkfield region, especially if all GPS data were included. The GPS measurements of the dense geodetic network there image a sharper transition of crustal velocities between blocks, and are interpreted as showing an anomalously shallow locking depth underneath that region. Another robust feature if we allowed for regional variations in d_1 was a shallow locking depth in the Salton Trough. The predicted slip rates for a regionally constant d_1 model are similar to those in Table 1, and the best-fitting d_1 model has also a similar slip-rate distribution (Fig. 10a). We defer further analysis of the relationship between best-fit d_1 and locking depth from seismicity, because a detailed regional model with more realistic fault geometries seems more appropriate for this purpose.

4.3 Comparison with palaeoseismology

In palaeoseismology, dated offsets of sedimentary strata are used to unravel the time dependence of slip events, and the overall fault slip rate at isolated trench sites (e.g. Sieh & Jahns 1984; Rockwell *et al.* 2000; McGill *et al.* 2002). It is therefore important to compare our present-day, interseismically derived fault slip rates with palaeoseismological constraints. However, there need not be a one-to-one correspondence between the slip rates from the two methods, especially when geomorphological studies that consider timescales larger than ~ 10 earthquake recurrence times are included. Among the possible reasons for deviations are progressive changes in earthquake recurrence time (e.g. Becker & Schmeling 1998; Marone 1998; Bonafede & Neri 2000), earthquake clustering (e.g. Sieh *et al.* 1989; Ward & Goes 1993; Rockwell *et al.* 2000; Friedrich *et al.* 2003), fault reorientation over geological timescales, and viscoelastic effects (e.g. Bonafede *et al.* 1986; Savage & Lisowski 1998), to name a few.

Table 1 compares our predicted fault slip rates for $\beta = 0$ and $\beta = 1$ with selected palaeoseismological and geomorphological rate estimates (see Table caption for references). This comparison should

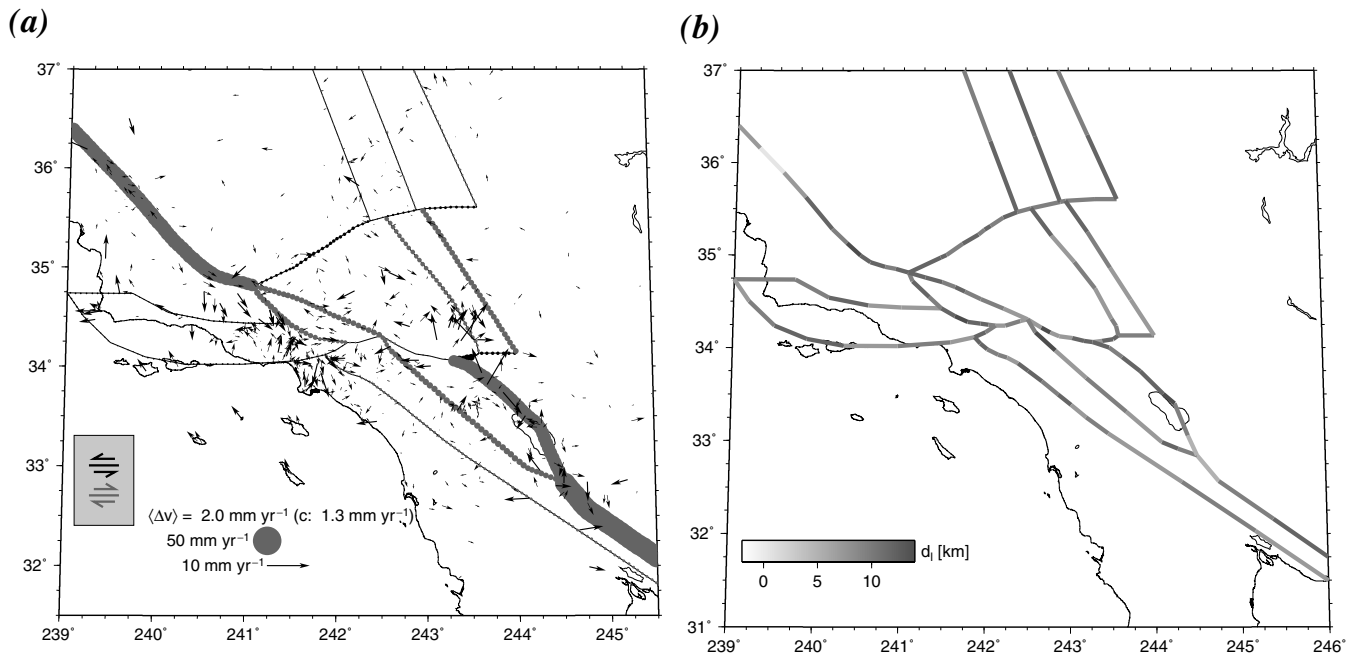


Figure 10. Residual GPS velocities Δv^i and predicted fault slip rates for (a) $\beta = 0$ with optimized d_1 (compare with Fig. 5), and (b) corresponding best-fit locking depths, d_1 . Locking depths were adjusted for 50-km-length subdivisions of faults using a Monte Carlo inversion.

be considered as an initial test only, and a more detailed exploration of the similarities and differences between geodetic and geological rates will require a more realistic fault geometry. However, we find good agreement between our rates and those from geology for the southern part of the San Andreas system (Elsinore, SJF, and SAF Indio). The largest discrepancy is the SBM segment, which we find to be hardly slipping at all, but for which palaeoseismology yields at least 15 mm yr^{-1} . The SAF Mojave section is also slower in our models than is geologically observed, by $\sim 8 \text{ mm yr}^{-1}$ ($\beta = 1$) and $\sim 15 \text{ mm yr}^{-1}$ ($\beta = 0$). The block models shift the missing right-lateral slip to the fault segments further to the west (Figs 5a and 7a). (This effect is less pronounced and the SAF Mojave moves at $\sim 15 \text{ mm yr}^{-1}$ for $\beta = 0$ if no normal motions on faults are allowed.) We also find some lag in the left-lateral slip on the Garlock segment, $\sim 4 \text{ mm yr}^{-1}$, compared with the geological rate of $\sim 7 \text{ mm yr}^{-1}$, which is, however, within the uncertainties of our model. In the north, the SAF Carrizo segment moves at the geological rate for $\beta = 0$ but is $\sim 7 \text{ mm yr}^{-1}$ slower for our $\beta = 1$ models.

For a better understanding of fault mechanics in general and the workings of the southern SAF in particular, it will be most instructive to study the disagreement between palaeoseismology and short-term, interseismic moment release. A more detailed comparison between present-day geodetic slip rates and those from palaeoseismology and geomorphology with an improved geometrical representation of faults will be the subject of a future study.

4.4 Effect of Landers

So far, we have only used the stress data set up to the 1992 Landers event. Fig. 11 shows the stresses from a focal mechanism inversion and a $\beta = 1$ block fault-slip model, if we include the whole catalogue data from 1992 up to 1999 in the stress inversion, and base our block model on this additional data set. Results can be compared with Figs 2(b) and 6(b). First, more grid cells are filled in the stress inversion results because there are more data. Second, we find clock-

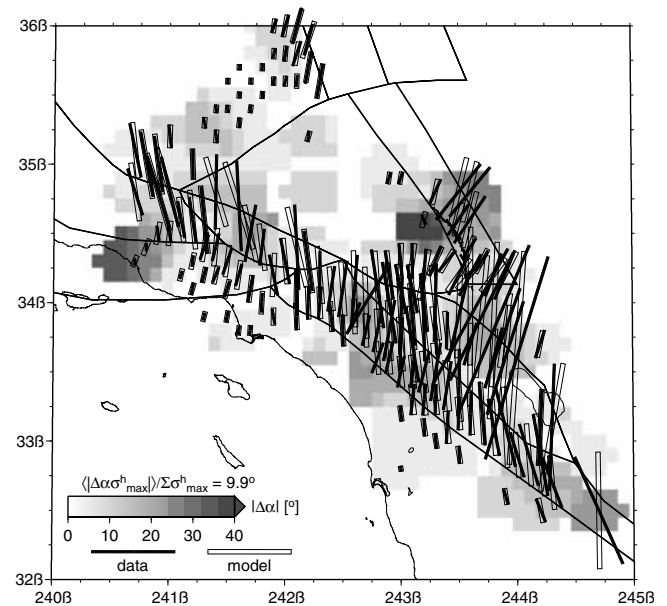


Figure 11. Horizontal components of scaled stresses from an inversion including focal mechanisms after Landers (filled sticks, compare with Fig. 2b) and model predictions (open sticks) for $\beta = 1$ ($\chi^2 = 4.6$). For explanation, see the caption to Fig. 6, and compare with results in Fig. 6(b).

wise rotation of the observed compressive axes with respect to the pre-Landers data set in a region on and south of the Landers surface rupture. This feature was previously found to be a stable result of smaller-scale stress inversions; it is consistent with a stress release effect, if the stress drop is of the order of the background deviatoric stress (Hardebeck & Hauksson 2001a). Comparing Figs 6(b) and 11, we note that our model fit to the longer-term data set deteriorates around Landers because predicted stresses are more north-south, and thus presumably closer to the long-term, background loading.

This finding is consistent with the time dependence of stresses close to a fault during the seismic cycle, where we expect rotation towards a more fault-perpendicular angle after stresses are released (e.g. Hardebeck & Hauksson 2001a). In this sense, and if focal mechanism inversions find the stress tensor, we can interpret the large angular misfit (α from our model rotated counter-clockwise with respect to inversion stress) that we see in the Landers region for the post-rupture data set in Fig. 11 as showing a fault far from failure. Depending on the assumptions about the stress-drop magnitude with respect to the background stress, this rotatight, however, not persist for a significant fraction of the seismic cycle. If the seismicity inversions find the stressing rate (Smith & Heaton 2003), we could expect a regionally modified loading signal after Landers while the stressing state returns to normal. We do not mean to suggest that $\Delta\alpha$ is a measure of seismic hazard, but we hope that such misfits (perhaps including time dependence) can give better insights into the behaviour of faults.

4.5 Effect of fault geometry variation

Even if we assume that our simplified description of crustal deformation is appropriate, fault slip rates will still depend on the choice of surface fault traces, fault dip angles, and the number and geometry of blocks in general. While surface traces of faults in southern California have been mapped in great detail (e.g. Jennings 1975), there are large ambiguities involved in determining if faults are presently active or not. There has been some progress recently in using seismic survey data to map faults without surface expressions (e.g. Shaw & Shearer 1999; Plesch *et al.* 2002), but we are far from a comprehensive 3-D model of active fault structures.

To explore the dependence of model results on block geometry, we show as an example strike-slip rates for a $\beta = 1$ joint inversion with an alternative block geometry around the San Bernardino mountains (Fig. 12). The alternative geometry has two additional,

hypothetical, faults in the SBM region, which were inferred based on topography (northern addition) and from seismicity (northwesterly trending structure).

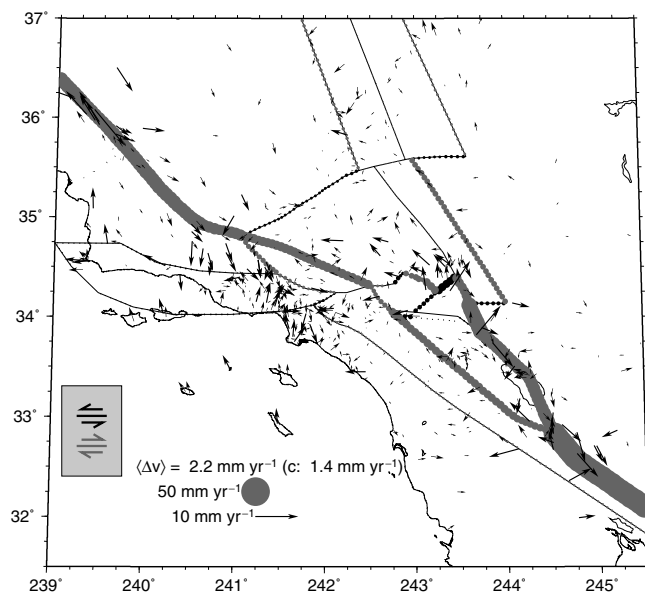
As expected for the increased number of free parameters, the misfit is improved for the more complicated geometry (compare Figs 7 and 12), in terms of both the GPS ($\chi^2_V = 3110$) and the stress misfit ($(|\Delta\alpha\sigma_{\max}^h|)/\sum\sigma_{\max}^h = 8^\circ$) for $\beta = 1$ compared with the simpler geometry. Individual faults in the proximity of SBM show modified slip rates; for example, compressive motion is now shifted towards the northern SBM region. However, the SBM section of the SAF is still predicted to be slipping very slowly, and the long-range effect in changing slip rates is minor. This indicates that the system does not depend critically on details, and that the inversion is robust for the damping we have chosen.

4.6 Comparison with other studies

Smith & Sandwell (2003) have modelled geodetic data, including the Shen *et al.* (2003) SCEC velocities, along the SAF with focus on Coulomb stress accumulation. Given the different objective of their model, Smith & Sandwell's fault geometry in southern California is much simpler than ours, and the only additional segment besides the main strand of the SAF in Smith & Sandwell's geometry is the San Jacinto fault. It is therefore difficult to compare slip rates or inverted locking depths. If we compare the uplift rates that are associated with bends in the fault geometry and normal motion, our model is consistent with Smith & Sandwell's (2003) results in that we predict subsidence in the Salton Trough and uplift around Tejon Pass, although our model predicts maximum uplift in the SBM area and some distributed shortening and uplift around the Transverse Ranges.

Our approach was inspired by Meade *et al.* (2002a), and this study is therefore much closer to our model; our $\beta = 0$ model differs from Meade *et al.*'s study mostly by the data selection and fault geometry.

(a) strike-slip



(b) normal

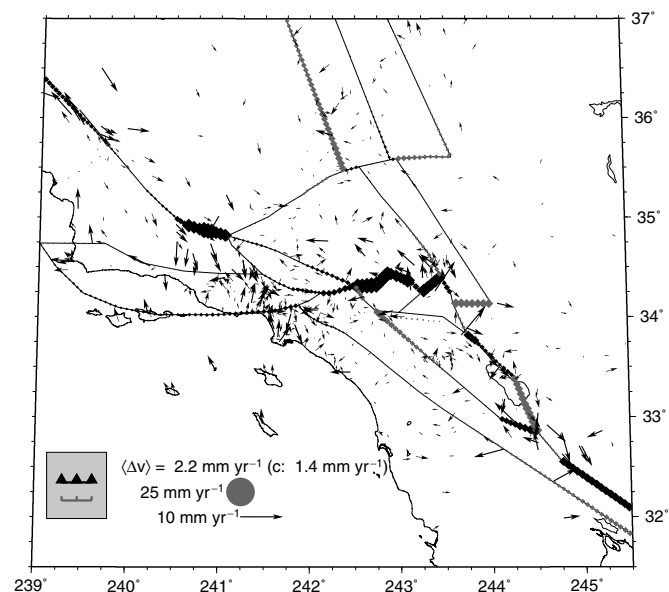


Figure 12. Residual GPS velocities Δv and predicted fault slip rates for a joint $\beta = 1$ inversion using an alternative fault geometry in the SBM region (compare with Fig. 7). Misfits for this model are $\chi^2_V = 3110$, $\chi^2_\tau = 17402$, and $\hat{\chi}^2 = 3.5$, compared with $\hat{\chi}^2 = 3.9$ for the simpler geometry as shown in Fig. 7. Weighted angular misfits of stress orientations, $(|\Delta\alpha\sigma_{\max}^h|)/\sum\sigma_{\max}^h$, are 8.6° and 8° for $\beta = 0$ and $\beta = 1$, respectively.

Our strike-slip rates agree with Meade *et al.*'s interpretation in that a significant part of the plate boundary motion in the centre and northern regions is taken up on the ECSZ and the Basin and Range faults. In both models, there is little slip on the Elsinore and San Bernardino segments of the SAF. A discrepancy between the models, which could be due to the different choices of fault geometry, is that we find more slip on the SAF Indio than on the San Jacinto, whereas the reverse is true for Meade *et al.* (2002a).

Fay & Humphreys (2003) have also used Shen *et al.*'s (2003) velocity solution to evaluate the partitioning of slip between SAF Indio, SJF, and Elsinore in the Salton Trough region. Since this region has a large sediment layer, Fay & Humphreys (2003) compared the slip-rate predictions from a finite-element model with lateral material heterogeneities with those from a homogeneous Okada (1992)-type solution. As in Bennett *et al.* (1996) and our block model, Fay & Humphreys found higher slip rates along the SAF Indio segment than along the SJF. A direct comparison with Bourne *et al.*'s (1998) method of deriving relative block motions by averaging geodetic velocities in segments across the plate boundary is problematic because it does not take the differences in fault models into account. However, our study roughly confirms the slip-rate partitioning of 6/12/22 mm yr⁻¹ that Bourne *et al.* (1998) found for the Elsinore/SJF/SAF Indio faults.

Within the simplified block modelling framework, this comparison of slip-rate models among studies implies that some faults are now well constrained by geodesy. Others, however, such as in the SBM region (Section 4.5), are strongly dependent on the exact choices of fault geometry. This ambiguity is perhaps not too surprising given the complexity of the SAF in these regions. We should, however, be cautious with the interpretation of GPS data, which are still not dense enough to narrow down fault mechanics to the required degree.

5 CONCLUSIONS

Block models such as that of Meade *et al.* (2002a) and the one we have introduced in this paper yield slip-rate estimates for southern California that can be interpreted as showing the present-day deformation partitioning between faults. Some regions are already fairly well constrained by geodesy, and where there are not enough GPS data other evidence such as stress from focal mechanisms can be brought to bear on the problem. In particular, we determine ~15 mm yr⁻¹ and ~23 mm yr⁻¹ of long-term slip on the SJF and the Indio segment of the SAF, respectively, accompanied by a low slip rate on the San Bernardino segment of the SAF.

We have shown that a physical model that is broadly consistent with interseismic velocities and stress from seismicity can be constructed. Further exploration of the model's successes and, more interestingly, its failures seems promising. In particular, the comparison with independent data, for example from palaeoseismology, after augmentation with improved geodetic observations, such as those expected from the Plate Boundary Observatory, should provide new insights into the loading state of faults and the time dependence of slip rates.

ACKNOWLEDGMENTS

This manuscript benefited from detailed and constructive reviews by Rick Bennett and Peter Clarke. We also thank Tom Rockwell for providing comments on palaeoseismological results for southern California, and for pointing out some of the intricacies of trenching in the trenches. Brendan Meade kindly shared many of his insights into block modelling and geodetic data with us. Bill Hammond,

Jim Savage and Duncan Agnew provided helpful comments on an earlier version of this manuscript. Most figures were produced with the GMT software by Wessel & Smith (1991). TWB was partly supported by the Cecil H. and Ida M. Green Foundation at IGPP, UCSD, and NSF grants EAR-0001046 and EAR-0112289.

REFERENCES

- Beanland, S. & Clark, M.M., 1993. Late Quaternary history of the Owens Valley fault zone, eastern California, and surface rupture associated with the 1872 earthquake (abstract), in *89th Ann. Mtg. Geol. Soc. Am., Cordilleran Section, Abstracts with Programs*, Vol. 25, 5(199304), 7. Geological Society of America, Boulder, CO, USA.
- Becker, T.W. & Schmelting, H., 1998. Earthquake recurrence time variations with and without fault zone interactions, *Geophys. J. Int.*, **135**, 165–176.
- Bennett, R.A., Rodi, W. & Reilinger, R.E., 1996. Global Positioning System constraints on fault slip rates in southern California and northern Baja, *J. geophys. Res.*, **101**, 21 943–21 960.
- Bennett, R.A., Davis, J.L. & Wernicke, B.P., 1999. Present-day pattern of cordilleran deformation in the western United States, *Geology*, **27**, 371–374.
- Bonafede, M. & Neri, A., 2000. Effects induced by an earthquake on its fault plane: a boundary element study, *Geophys. J. Int.*, **141**, 43–56.
- Bonafede, M., Dragoni, M. & Morelli, A., 1986. On the existence of a periodic dislocation cycle in horizontally layered viscoelastic model, *J. geophys. Res.*, **91**, 6396–6404.
- Bourne, S.J., England, P.C. & Parsons, B., 1998. The motion of crustal blocks driven by flow of the lower lithosphere and implications for slip rates of continental strike-slip faults, *Nature*, **391**, 655–659.
- Brown, R.D., 1990. Quaternary deformation, in *The San Andreas Fault System, California*, Vol. 1515, *US Geol. Surv. Prof. Pap.*, pp. 83–113, US Geol. Surv., Boulder.
- Crook, R.J., Allen, C.R., Kamb, B., Payne, C.M. & Proctor, R.J., 1987. Quaternary geology and seismic hazard of the Sierra Madre and associated faults, western San Gabriel Mountains, in *Recent Reverse Faulting in the Transverse Ranges, California*, Vol. 1339, *US Geol. Surv. Prof. Pap.*, pp. 27–63, US Geol. Surv., Boulder.
- DeMets, C., Gordon, R.G., Argus, D.F. & Stein, S., 1994. Effect of recent revisions to the geomagnetic reversal time scale on estimates of current plate motions, *Geophys. Res. Lett.*, **21**, 2191–2194.
- Deng, J., Gurnis, M., Kanamori, H. & Hauksson, E., 1998. Viscoelastic flow in the lower crust after the 1992 Landers, California, earthquake, *Science*, **282**, 1689–1692.
- Dixon, T.H., Norabuena, E. & Hotaling, L., 2003. Paleoseismology and Global Positioning System; earthquake-cycle effects and geodetic versus geologic fault slip rates in the Eastern California shear zone, *Geology*, **31**, 55–58.
- Dokka, R.K. & Travis, C.J., 1990. Role of the eastern California shear zone in accommodating Pacific–North American plate motion, *Geophys. Res. Lett.*, **17**, 1323–1326.
- Dolan, J.F., Sieh, K.E., Rockwell, T.K., Yeats, R.S., Shaw, J., Suppe, J., Huftile, G.J. & Gath, E.M., 1995. Prospects for larger or more frequent earthquakes in the Los Angeles metropolitan region, *Science*, **267**, 199–205.
- Dolan, J.F., Sieh, K.E. & Rockwell, T.K., 2000. Late Quaternary activity and seismic potential of the Santa Monica fault system, Los Angeles, California, *Geol. soc. Am. Bull.*, **112**, 1559–1581.
- Dorsey, R.J., 2002. Stratigraphic record of Pleistocene initiation and slip on the Coyote Creek Fault, lower Coyote Creek, Southern California, in *Contributions to Crustal Evolution of the Southwestern United States*, **365**, pp. 251–269, ed. Barth, A., Special Paper, Geological Society of America, Boulder, CO, USA.
- Dorsey, R.J., 2003. Late pleistocene slip rate on the Coachella Valley segment of the San Andreas fault and implications for regional slip partitioning (abstract), in *99th Ann. Mtg. Cordilleran Section, Abstracts with Programs*, Vol. 35, 4(200304), 22. Geological Society of America, Boulder, CO, USA.

- Drewes, H., 1998. Combination of VLBI, SLR and GPS determined station velocities for actual plate kinematic and crustal deformation models, in *Geodynamics*, eds Forsberg, R., Feissel, M. & Dietrich, R., International Association of Geodesy Symposia, Vol. 119, pp. 377–382, Springer-Verlag, New York.
- England, P.C. & Molnar, P., 1997. Active deformation of Asia: from kinematics to dynamics, *Science*, **278**, 647–650.
- Fay, N.P. & Humphreys, E.D., 2003. Pacific–North America plate boundary deformation in the greater Salton Trough area, southern California, USA (abstract), *EOS, Trans. Am. geophys. Un.*, **84**, T51A-07.
- Flesch, L.M., Holt, W.E., Haines, A.J. & Bingmin, S.-T., 2000. Dynamics of the Pacific–North American plate boundary in the western United States, *Science*, **287**, 834–836.
- Friedrich, A.M., Wernicke, B., Niemi, N.A., Bennett, R.A. & Davis, J.L., 2003. Comparison of geodetic and geologic data from the Wasatch region, Utah, and implications for the spectral character of Earth deformation at periods of 10 to 10 million years, *J. geophys. Res.*, **108**, doi:10.1029/2001JB000682.
- Gordon, R.G., 2000. Diffuse oceanic plate boundaries: Strain rates, vertically averaged rheology, and comparisons with narrow plate boundaries and stable plate interiors, in *The History and Dynamics of Global Plate Motion*, Vol. 121, pp. 143–159, eds Richards, M.A., Gordon, R.G. & van der Hilst, R.D., Geophysical Monograph, Am. Geophys. Un., Washington DC.
- Hardebeck, J.L. & Hauksson, E., 2001a. Crustal stress field in southern California and its implications for fault mechanics, *J. geophys. Res.*, **106**, 21 859–21 882.
- Hardebeck, J.L. & Hauksson, E., 2001b. Stress orientations obtained from earthquake focal mechanisms; what are appropriate uncertainty estimates?, *Bull. seism. Soc. Am.*, **91**, 250–262.
- Hardebeck, J.L. & Shearer, P.M., 2002. A new method for determining first-motion focal mechanisms, *Bull. seism. Soc. Am.*, **92**, 2264–2276.
- Harden, J.W. & Matti, J.C., 1989. Holocene and late Pleistocene slip rates on the San Andreas Fault in Yucaipa, California, using displaced alluvial-fan deposits and soil chronology, *Geol. soc. Am. Bull.*, **101**, 1107–1117.
- Hauksson, E., 2000. Crustal structure and seismicity distribution adjacent to the Pacific and North America plate boundary in southern California, *J. geophys. Res.*, **105**, 13 875–13 903.
- Hitchcock, C., Lindvall, S.C., Treiman, J.A., Weaver-Bowman, K., Helms, J.G., Lettis, W.R. & Simpson, G.D., 2003. Paleoseismic investigation of the Simi fault at Arroyo Simi, Simi Valley, CA: Evidence for timing of Late Holocene earthquakes on the Simi-Santa Rosa fault zone, *Bull. seism. Soc. Am.*, in press.
- Jennings, C.W., 1975. *Fault map of California with Locations of Volcanoes, Thermal Springs, and Thermal Wells*, No. 1 in Geologic Data Map, California Division of Mines and Geology, Sacramento CA.
- Johnson, H.O., 1993. Techniques and studies in crustal deformation, *PhD thesis*, University of California, San Diego.
- Kaufman, P.S. & Royden, L.H., 1994. Lower crustal flow in an extensional setting; constraints from the Halloran Hills region, eastern Mojave Desert, California, *J. geophys. Res.*, **99**, 15 723–15 739.
- Keller, E.A., Bonkowski, M.S., Korsh, R.J. & Shlemon, R.J., 1982. Tectonic geomorphology of the San Andreas fault zone in the southern Indio Hills, Coachella Valley, California, *Geol. soc. Am. Bull.*, **93**, 46–56.
- Kendrick, K.J., Morton, D.M., Wells, S.G. & Simpson, R.W., 2002. Spatial and temporal deformation along the northern San Jacinto Fault, Southern California; implications for slip rates, *Bull. seism. Soc. Am.*, **92**, 2782–2802.
- Kostrov, B.V., 1974. Seismic moment and energy of earthquakes and seismic flow of rock, *Izv. Acad. Sci., USSR, Phys. Solid Earth* (English Translation), **1**, 13–21.
- Kreemer, C., Holt, W.E. & Haines, A.J., 2003. An integrated global model of present-day plate motions and plate boundary deformation, *Geophys. J. Int.*, **154**, 5–34.
- Lee, J., Rubin, C., Miller, M., Spencer, J., Lewis, O. & Dixon, T., 2000. Kinematics of the Eastern California shear zone north of the Garlock Fault (Abstract), in *2000 Ann. Mtg. Geol. Soc. Am., Abstracts with Programs*, Vol. 32, 7(2000), 105. Geological Society of America, Boulder, CO, USA.
- McClusky, S. *et al.*, 2000. Global Positioning System constraints on plate kinematics and dynamics in the eastern Mediterranean and Caucasus, *J. geophys. Res.*, **105**, 5695–5719.
- McClusky, S.C., Bjornstad, S.C., Hager, B.H., King, R.W., Meade, B.J., Miller, M.M., Monastero, F.C. & Souter, B.J., 2001. Present day kinematics of the Eastern California shear zone from a geodetically constrained block model, *Geophys. Res. Lett.*, **28**, 3369–3372.
- McGill, J.T., 1989. Geologic maps of the Pacific Palisades area, Los Angeles, California, in *Map I-1828, Miscellaneous Investigations Series*, Vol. 1:4, p. 800, US Geol. Surv., Reston, VA, USA.
- McGill, S.F. & Sieh, K.E., 1993. Holocene Slip Rate of the Central Garlock Fault in Southeastern Searles Valley, *J. geophys. Res.*, **98**, 14 217–14 231.
- McGill, S. *et al.*, 2002. Paleoseismology of the San Andreas fault at Plunge Creek, near San Bernardino, Southern California, *Bull. seism. Soc. Am.*, **92**, 2803–2840.
- Magistrale, H. & Rockwell, T.K., 1996. The central and southern Elsinore fault zone, southern California, *Bull. seism. Soc. Am.*, **86**, 1793–1803.
- Marone, C., 1998. The effect of loading rate on static friction and the rate of fault healing during the earthquake cycle, *Nature*, **391**, 69–72.
- Meade, B.J., Hager, B.H. & King, R.W., 2002a. Block models of present day deformation in Southern California constrained by geodetic measurements (Abstract), *2002 SCEC Ann. Mtg.*, p. 96. Proceedings and Abstracts, Oxnard, CA. Southern California Earthquake Center, Los Angeles, CA, USA.
- Meade, B.J., Hager, B.H., McClusky, S.C., Reilinger, R.E., Ergintav, S., Lenk, O., Barka, A.A. & Ozener, H., 2002b. Estimates of seismic potential in the Marmara Sea region from block models of secular deformation constrained by Global Positioning System measurements, *Bull. seism. Soc. Am.*, **92**, 208–215.
- Michael, A.J., 1984. Determination of stress from slip data; faults and folds, *J. geophys. Res.*, **89**, 11 517–11 526.
- Michael, A.J., 1987. Use of focal mechanisms to determine stress; a control study, *J. geophys. Res.*, **92**, 357–368.
- Nostro, C., Piersanti, A., Antonioli, A. & Spada, G., 1999. Spherical versus flat models of coseismic and postseismic deformations, *J. geophys. Res.*, **104**, 13 115–13 134.
- Okada, Y., 1992. Internal deformation due to shear and tensile faults in a half-space, *Bull. seism. Soc. Am.*, **82**, 1018–1040.
- Peltzer, G., Crampe, E., Hensley, S. & Rosen, P.A., 2001. Transient strain accumulation and fault interaction in the Eastern California shear zone, *Geology*, **29**, 975–978.
- Plesch, A. *et al.*, 2002. SCEC 3D community fault model for southern California (abstract), *EOS, Trans. Am. geophys. Un.*, **83**, S21A–0966.
- Pollitz, F.F., 2003. The relationship between the instantaneous velocity field and the rate of moment release in the lithosphere, *Geophys. J. Int.*, **153**, 595–608.
- Pollitz, F.F., Wicks, C. & Thatcher, W., 2001. Mantle flow beneath a continental strike-slip fault: Postseismic deformation after the 1999 Hector Mine earthquake, *Science*, **293**, 1814–1818.
- Prentice, C.S., Weldon, R.J. & Sieh, K.E., 1986. Distribution of slip between the San Andreas and San Jacinto faults near San Bernardino, southern California (Abstract), in *82nd Ann. Mtg. Geol. Soc. Am., Cordilleran Section, Abstracts with Programs*, Vol. 18, 2(198602), 172. Geological Society of America, Boulder, CO, USA.
- Press, W.H., Teukolsky, S.A., Vetterling, W.T. & Flannery, B.P., 1993. *Numerical Recipes in C: The Art of Scientific Computing*, 2nd edn, Cambridge Univ. Press, Cambridge.
- Reinecker, J., Heidbach, O. & Müller, B., 2003. The 2003 release of the World Stress Map (available online at www.world-stress-map.org).
- Rockwell, T.K., 1988. Neotectonics of the San Cayetano Fault, Transverse Ranges, California, *Geol. soc. Am. Bull.*, **100**, 500–513.
- Rockwell, T.K., Loughman, C. & Merifield, P., 1990. Late Quaternary rate of slip along the San Jacinto fault zone near Anza, southern California, *J. geophys. Res.*, **95**, 8593–8605.
- Rockwell, T.K., Lindvall, S., Herzberg, M., Murbach, D., Dawson, T. & Berger, G., 2000. Paleoseismology of the Johnson Valley, Kickapoo, and Homestead Valley faults: clustering of earthquakes in the Eastern California Shear Zone, *Bull. seism. Soc. Am.*, **90**, 1200–1236.

- Savage, J.C., 1990. Equivalent strike-slip earthquake cycles in half-space and lithosphere–asthenosphere Earth models, *J. geophys. Res.*, **95**, 4873–4879.
- Savage, J. & Burford, R., 1973. Geodetic determination of relative plate motion in central California, *J. geophys. Res.*, **78**, 832–845.
- Savage, J. & Lisowski, M., 1998. Viscoelastic coupling model of the San Andreas fault along the Big Bend, Southern California, *J. geophys. Res.*, **103**, 7281–7289.
- Schroeder, J.M., Lee, J., Owen, L.A. & Finkel, R.C., 2002. Quaternary dextral fault slip history along the White Mountains fault zone, California (abstract), in *98th Ann. Mtg. Geol. Soc. Am., Cordilleran Section, Abstracts with Programs*, Vol. 34, 5(200204), 87. Geological Society of America, Boulder, CO, USA.
- Sharp, R.V., 1981. Variable rates of Late Quaternary strike-slip on the San Jacinto fault zone, *J. geophys. Res.*, **86**, 1754–1762.
- Shaw, J.H. & Shearer, P.M., 1999. An elusive blind-thrust fault beneath metropolitan Los Angeles, *Science*, **283**, 1516–1518.
- Shen, Z.-K. *et al.*, 2003. *The SCEC Crustal Motion Map*, version 3.0, available online at <http://epicenter.usc.edu/cmm3/>.
- Sheridan, J.M. & Ben-Zion, Y., 2000. High-resolution strain variability in southern California from analysis of 80,000 earthquakes (Abstract), *EOS, Trans. Am. geophys. Un.*, **81**, S22A–06.
- Sieh, K.E. & Jahns, R., 1984. Holocene activity of the San Andreas fault at Wallace Creek, California, *Geol. Soc. Am. Bull.*, **95**, 883–896.
- Sieh, K.E., Stuiver, M. & Brillinger, D., 1989. A more precise chronology of earthquakes produced by the San Andreas fault in Southern California, *J. geophys. Res.*, **94**, 603–623.
- Smith, D.E. & Heaton, T.H., 2003. Interpreting focal mechanisms in a heterogeneous stress field (Abstract), *EOS, Trans. Am. geophys. Un.*, **84**, S41C–0105.
- Smith, B. & Sandwell, D., 2003. Coulomb stress accumulation along the San Andreas fault system, *J. geophys. Res.*, **108**, 2296, doi:10.1029/2002JB002136.
- Spakman, W. & Nyst, M. C.J., 2002. Inversion of relative motion data for estimates of the velocity gradient field and fault slip, *Earth planet. Sci. Lett.*, **203**, 577–591.
- Stein, S., 1993. Space geodesy and plate motions, in *Contributions of Space Geodesy to Geodynamics: Crustal Dynamics*, Vol. 23, pp. 5–20, eds Smith, D.E. & Turcotte, D.L., Geodynamics, Am. Geophys. Un., Washington, DC.
- Thomas, A.P. & Rockwell, T.K., 1996. A 300- to 550-year history of slip on the Imperial Fault near the US-Mexico border; missing slip at the Imperial Fault bottleneck, *J. geophys. Res.*, **101**, 5587–5997.
- Treiman, J.A., 1994. Geomorphic clues to paleoseismicity; examples from the eastern Ventura Basin, Los Angeles County, California, in *Proc. Workshop on Paleoseismology*, pp. 182–184, eds Prentice, C.S., Schwartz, D.P. & Yeats, R.S., Open-File Report, OF 94-0568, US Geol. Surv., Reston, VA, USA.
- van der Woerd, J., Klinger, Y., Sieh, K.E., Tapponnier, P. & Ryerson, F., 2001. First long-term slip-rate along the San Andreas Fault based on ^{10}Be - ^{26}Al surface exposure dating: The Biskra Palms site, 23 mm yr $^{-1}$ for the last 30,000 years (Abstract), *EOS, Trans. Am. geophys. Un.*, **82**, S52D–0673.
- Vaughan, P.R., Thorup, K.M. & Rockwell, T.K., 1999. Paleoseismology of the Elsinore Fault at Agua Tibia Mountain, southern California, *Bull. seism. Soc. Am.*, **89**, 1447–1457.
- Walls, C., Rockwell, T.K., Pfanner, J., Bornyax, M. & Lindvall, S., 1997. Uplift gradient along the Sierra Madre-Cucamonga fault zone, Los Angeles, California (Abstract), in *Geol. Soc. Am., Cordilleran Section, Abstracts with Programs*, Vol. 29, 5(199704), 72. Geological Society of America, Boulder, CO, USA.
- Ward, S.N. & Goes, S. D.B., 1993. How regularly do earthquakes recur? A synthetic seismicity model for the San Andreas fault, *Geophys. Res. Lett.*, **20**, 2131–2134.
- Wdowinski, S., Sudman, Y. & Bock, Y., 2001. Geodetic detection of active faults in S. California, *Geophys. Res. Lett.*, **28**, 2321–2324.
- Weldon, R.J. & Sieh, K.E., 1985. Holocene rate of slip and tentative recurrence interval for large earthquakes on the San Andreas Fault, Cajon Pass, Southern California, *Geol. Soc. Am. Bull.*, **96**, 793–812.
- Wessel, P. & Smith, W.H.F., 1991. Free software helps map and display data, *EOS, Trans. Am. geophys. Un.*, **72**, 445–446.
- Zoback, M.L., 1992. First- and second-order patterns of stress in the lithosphere: The World Stress Map project, *J. geophys. Res.*, **97**, 11 703–11 728.

APPENDIX A: VELOCITY DATA SELECTION

Besides excluding post-seismic transients of Landers (all data points denoted by ‘GLA’ in SCEC3 but BEAR and MILU), removing the outliers flagged by Shen *et al.* (2003) with ‘?’, excluding all VLBI and all EDM data but RICU and WARR, we exclude the following stations, either because we consider them outliers or because they are spatially clustered: 33JD, 7085, BREK, CAND, CARR, CASO, CIC1, CP13, CPEI, D138, ECRK, G109, G114, G120, G123, G124, G125, G128, G134, GOLD, ISLK, JOAQ, JPLA, JPLM, LAND, M586, MASO, MDAY, MIDA, MIDE, MNMT, MOJ1, MOJA, MOJM, MONT, OQUI, PAXU, PIN1, PIN3, POMM, ROUN, SIO2, WKPK, and X138.

Table A1. Euler solution vectors for the long-term motion, ω^i , of all blocks as shown in Fig. 1 for GPS-only ($\beta = 0$, Fig. 5) and joint ($\beta = 1$, Fig. 7) inversion. The ω^i are specified in a Cartesian system with respect to block L (x , y , and z are axes at $0^\circ\text{E}/0^\circ\text{N}$, $90^\circ\text{E}/0^\circ\text{N}$, and the geographic North pole, 90°N , respectively). Uncertainties are σ_ω from eq. (7), and all values are in $^\circ\text{Myr}^{-1}$. The ω^L that was subtracted is $(-0.16 \pm 0.02, -0.34 \pm 0.04, 0.25 \pm 0.03)$ for $\beta = 0$ and $(-0.11 \pm 0.02, -0.24 \pm 0.04, 0.17 \pm 0.03)$ for $\beta = 1$ in the original SCEC reference frame (\pm ranges indicate 1σ). Numbers for ω^i can be compared with the NUVEL-1A Euler pole for the Pacific with respect to North America: $\omega^{\text{PAC-NAM}} = (-0.101, 0.483, -0.562)$ (DeMets *et al.* 1994), or the geodesy-based estimate of $\omega^{\text{PAC-NAM}} = (-0.102, 0.474, -0.595)$ (Kreemer *et al.* 2003).

Block code i	$\beta = 0$ inversion			$\beta = 1$ inversion		
	ω_x^i	ω_y^i	ω_z^i	ω_x^i	ω_y^i	ω_z^i
A	0.42 ± 0.04	0.96 ± 0.08	-0.84 ± 0.07	0.15 ± 0.03	0.53 ± 0.06	-0.51 ± 0.05
B	0.29 ± 0.06	0.70 ± 0.12	-0.63 ± 0.10	0.03 ± 0.06	0.21 ± 0.11	-0.17 ± 0.09
C	0.64 ± 0.06	1.35 ± 0.12	-1.13 ± 0.10	0.60 ± 0.06	1.26 ± 0.12	-1.06 ± 0.10
D	0.60 ± 0.05	1.76 ± 0.09	-1.62 ± 0.08	0.81 ± 0.05	2.06 ± 0.09	-1.86 ± 0.07
E	0.13 ± 0.07	0.64 ± 0.13	-0.69 ± 0.10	-0.00 ± 0.07	0.41 ± 0.13	-0.52 ± 0.10
F	0.79 ± 0.06	1.84 ± 0.11	-1.52 ± 0.09	0.61 ± 0.04	1.41 ± 0.08	-1.17 ± 0.06
G	0.14 ± 0.06	0.49 ± 0.13	-0.43 ± 0.10	0.09 ± 0.06	0.34 ± 0.12	-0.29 ± 0.09
H	0.72 ± 0.07	1.88 ± 0.12	-1.68 ± 0.09	0.59 ± 0.06	1.65 ± 0.11	-1.49 ± 0.09
I	-0.24 ± 0.05	0.09 ± 0.10	-0.28 ± 0.07	-0.28 ± 0.04	0.02 ± 0.08	-0.20 ± 0.06
J	0.60 ± 0.06	1.62 ± 0.13	-1.29 ± 0.09	0.43 ± 0.06	1.27 ± 0.11	-1.03 ± 0.08
K	0.12 ± 0.02	0.90 ± 0.04	-0.87 ± 0.03	0.12 ± 0.02	0.84 ± 0.04	-0.84 ± 0.03

Table A2. Geographic representation of Euler vectors, ω , with respect to block L as converted from Table A1. The ω^L as used for reference are (65.01°E, -33.95°N, -0.45° Myr⁻¹) for $\beta = 0$; (64.38°E, -33.33°N, -0.32° Myr⁻¹) for $\beta = 1$; and (70.92°E, -40.99°N, 0.29° Myr⁻¹) for ω_r^L , all in the original SCEC reference frame. Compare the relative ω in the Table (amplitudes are in ° Myr⁻¹) with the NUVEL1-A pole of the Pacific with respect to North America: $\omega^{\text{PAC-NAM}} = (101.81^\circ\text{E}, -48.72^\circ\text{N}, 0.75^\circ\text{ Myr}^{-1})$ (DeMets *et al.* 1994).

Block code <i>i</i>	$\beta = 0$ inversion		$\beta = 1$ inversion		best-fit rigid block	
	lon. [°E], lat. [°N]	$ \omega $	lon. [°E], lat. [°N]	$ \omega $	lon. [°E], lat. [°N]	$ \omega $
A	66.6, -38.7	1.34	74.1, -42.5	0.75	64.2, -38.0	2.01
B	67.5, -39.6	0.99	82.5, -39.7	0.27	72.6, -46.3	0.25
C	64.6, -37.0	1.88	64.3, -37.4	1.75	63.2, -37.3	1.31
D	71.1, -41.0	2.47	68.5, -40.1	2.89	68.8, -41.0	1.88
E	78.4, -46.2	0.95	90.4, -51.6	0.66	138.2, -55.1	0.28
F	66.8, -37.2	2.52	66.6, -37.4	1.93	66.6, -37.4	1.82
G	74.0, -39.9	0.66	75.7, -39.6	0.45	131.2, -49.3	0.07
H	69.1, -39.8	2.62	70.4, -40.5	2.30	72.2, -41.8	1.54
I	160.2, -46.7	0.38	176.4, -35.1	0.35	49.4, -21.8	-0.89
J	69.6, -36.7	2.16	71.4, -37.4	1.69	71.7, -38.0	1.21
K	82.1, -43.9	1.26	82.2, -44.6	1.19	96.5, -49.0	0.62